

Analysis of neutron diffraction by optically thin grating

*A study of a neutron diffraction experiment with
nanoparticle-polymer composite gratings outside of
the Bragg regime*

Student:
Ismaele Vincent
Masiello

Supervisors:
Simon Wall¹
Jürgen Klepp²

A thesis presented for the master's degree in
Physics



Department of physics and astronomy
Aarhus University
Denmark

Academic year 2021/2022

¹Department of Physics and Astronomy, University of Aarhus, Ny Munkegade, Building 1520, DK-8000 Aarhus C, Denmark

²University of Vienna, Faculty of physics, Boltzmanngasse 5, 1090 Vienna, Austria

Acknowledgements

To Samira, without you this last year would have not been as special as it was. Thank you for supporting me during difficult times, and for sharing with me the moments of joy.

To Francesco, despite not being fellow students anymore, we never stopped studying together as if we still were in those first years of university. Most importantly, we never stopped being friends.

To my friends, my family, and all the people in my life that, intentionally or unintentionally, positively contributed to make me the person I am now. In particular, vielen Dank M. Emes.

Finally, last but by no means least, I would like to express my most sincere gratitude to Jürgen Klepp and Martin Fally from the University of Vienna, and Simon Wall from the University of Århus. Thank you for giving me the chance to carry out this master's thesis project and for providing fundamental support throughout the whole process.

Analysis of neutron diffraction by optically thin grating

A study of a neutron diffraction experiment with nanoparticle-polymer composite gratings outside of the Bragg regime

Ismaele Vincent Masiello

Abstract

Holographic gratings have been used for decades in different fields such as acousto-optics, integrated optics, holography, and spectroscopy [1], and due to the development in the production techniques and the new materials available they have become a very efficient and fairly easily customizable component for both neutron- and laser- optics [2].

A diffraction experiment with such gratings can lead to substantially different outcomes depending on thickness and modulation profile. Bragg regime gratings, also known as thick gratings, predominantly produce only two orders of diffracted waves (0th and 1st order) and the relative diffraction efficiencies are well described by two-coupled-waves theories. However, outside of the Bragg regime thinner gratings generate higher orders of diffraction that are not neglectable anymore [3] and therefore a different model is needed [4].

In this thesis, a set of data from a neutron diffraction experiment collected between 2012 and 2013 at the Institute Laue-Langevin (ILL) [5] in Grenoble (France) is analysed. An attempt of analysis has been carried out using two-coupled-waves (Bragg regime) theories which did not yield acceptable results. The data clearly show the presence of non-neglectable higher orders of diffracted waves and therefore a multi-coupled-wave approach is implemented.

Contents

1	Introduction	9
2	Theory	12
2.1	Rigorous Coupled Wave Theory for neutrons	12
2.1.1	Diffraction gratings with perfectly sinusoidal modulation of the refractive index	12
2.1.2	Diffraction gratings presenting additional Fourier components in the modulation of the refractive index . . .	19
2.1.3	Pendellösung interference	20
3	The experiment	24
3.1	The sample	24
3.2	The measurements	25
3.3	Experimental set-up	28
3.4	The instrument	28
4	Data analysis and discussion	30
4.1	Preliminary analysis	30
4.1.1	Shape, size and position of the spots	31
4.1.2	Diffracted spots	33
4.1.3	Neutron intensity	33
4.2	Diffraction efficiencies	35
4.2.1	Definition of the region of interest	35
4.2.2	Estimation of the incident angle of the measurements .	37
4.2.3	Neutron counts	39
4.2.4	Uncertainties	41
4.3	Observation of the Pendellösung interference	42
4.4	Wavelength distribution and beam divergence	43
4.4.1	Wavelength distribution	43
4.4.2	Beam divergence	44
4.5	Fits results	45

4.5.1	Perfectly sinusoidal grating with fixed wavelength distribution	46
4.5.2	Perfectly sinusoidal grating with free parameters for the wavelength distribution	48
4.5.3	Diffraction grating with two Fourier components in the modulation of the refractive index	53
5	Summary and conclusions	59
5.1	Experimental aspects	59
5.2	Analysis results	61
5.2.1	Diffraction efficiencies	61
5.2.2	Pendellösung interference	63
5.3	Conclusions	63
	Bibliography	65
A		69
A.1	Re-arranging of the coupled-waves sum	69
A.2	ROI search algorithm	70
A.3	Fit results according to the model presented in subsec. 4.5.3	71

List of Figures

1.1	Example of diffraction experiment in the Bragg regime (<i>left, optically thick grating</i>) and outside the Bragg regime (<i>right, optically grating</i>).	9
2.1	Diffraction scheme.	13
2.2	Geometry of the coupled wave-vectors. (N.B. the fading color of the diffraction grating is just to make the figure more readable, it has no physical meaning.)	16
2.3	Example of thickness modulation by tilt	21
2.4	Numerical simulations of the Pendellösung interference for different thicknesses (top) and three possible configurations (bottom): 50:50 beam splitter (left), mirror-like (center) and transmission (right).	21
2.5	Numerical simulation of a three-port beam splitter configuration.	22
2.6	Numerical simulation of Pendellösung interference for 0th, 1st, and 2nd order of diffraction.	23
2.7	Pendellösung interference for different tilt angles ζ	23
3.1	Interference setup used to obtain light of sinusoidal intensity profile at the sample position.	24
3.2	Mixture of nanoparticles and monomers before (top) and after (bottom) light-induced hologram recording.	25
3.3	Diffraction grating with sinusoidal modulation of the refractive index.	25
3.4	Modulation of the thickness of the diffraction grating by tilting.	26
3.5	Example of images from the measurement (contrast enhanced).	26
3.6	Example the neutron counts in each diffraction spot assigned to the different diffraction orders for step-wise variation of θ .	27
3.7	Top view of the diffraction plane.	28
3.8	Measured wavelength distribution by Blaickner et al. fitted by an exponentially modified Gaussian (EMG) [23].	29

4.1	Example of three measurements for different values of θ in 32-bit grey-scale format (cropped and with contrast enhanced.)	30
4.2	Plot of the average horizontal profile of the spot in the sampleless measurement.	31
4.3	Diffraction spots for three different tilt angles: $\zeta = 0^\circ$ (left), $\zeta = 69^\circ$ (center), and $\zeta = 80^\circ$ (right) (cropped and with contrast enhanced).	32
4.4	Example of spots overlap between 1st and 2nd diffraction orders for $\zeta = 40$ deg (left), with plot of the neutron counts profile (right).	33
4.5	Average neutron counts for all the collected measurement	34
4.6	Sum of measurements for tilt angle $\zeta = 77.88$ deg, with brightness and contrast enhanced.	34
4.7	3D array containing all the measurements θ_z for a measurement session of fixed tilt angle ζ .	36
4.8	Visual representation of the effect of the ROI search algorithm: (a) 2D projection on the (x, y) pixel plane of the maximum values along z , (b) Limiting rows of the ROI, and (c) final result. The discarded pixels are highlighted with a brighter shade.	37
4.9	Example of estimation of z_0 with $\theta_{z_0} = 0$ (using the 0th order of $\zeta = 40$ deg).	38
4.10	Example of estimation of z_0 with only one minimum ($\zeta = 80$ deg).	38
4.11	(a) Row intensity profile. (b) Fit with sum of Gaussian functions.	39
4.12	Location of diffracted peaks and overlapping region defined using the fit of sum of Gaussian distributions from equation 4.3.	40
4.13	Neutron counts outside of the ROI for sessions with different exposure times fitted with a Poisson distribution $P(k) = e^{-\mu} \frac{\mu^k}{k!}$.	41
4.14	Experimental observation of Pendellösung interference extracted from the analysed data set	42
4.15	Example of weighted sampling for a general Gaussian distribution (<i>left</i>) compared to uniform sampling (<i>right</i>) produced by the same number of points.	43
4.16	Example of inverse transform sampling.	44
4.17	Fit results for and $\zeta = 77.88$.	46
4.18	Fit results for $\zeta = 77.88$ with σ_{div} as additional free parameter.	47
4.19	Plot of the maximum diffraction efficiencies predicted for the orders -1 and -2 compared with experimental data, according to the model of subsection 4.5.1	48

4.20	Fit results for 1st and 2nd diffraction order with $\zeta = 40$ deg (top) and $\zeta = 48$ (bottom).	49
4.21	Wavelength distributions according to fit results for all measurements	49
4.22	Evolution of $\lambda_{mean/max}$ for different tilt angles according to fit results for group 3 (top), group 2 (center) and all measurements (bottom)	50
4.23	Fit results for the scattering length-density modulation parameter $b_c\Delta\rho_1$	51
4.24	Fit results for $\zeta = 75.64$ deg showing accentuated asymmetry for the 2nd diffraction order.	52
4.25	Intensity of 0th diffraction order spot for $\zeta = 75.64$ deg.	52
4.26	Plot of the maximum diffraction efficiencies predicted for the orders -1 and -2 compared with experimental data, according to the model presented in subsection 4.5.2	53
4.27	Fit results for 1st and 2nd diffraction order with $\zeta = 79$ deg, for one (top) and two (bottom) Fourier components of the refractive index modulation.	54
4.28	Fit results for $\zeta = 77.88$ deg.	54
4.29	Wavelength distributions according to fit results for all measurements (top) and for $\zeta = 40$ deg (bottom).	55
4.30	Evolution of $\lambda_{mean/max}$ for different tilt angles according to fit results for group 3 (top), group 2 (center) and all measurements (bottom)	56
4.31	Fit results for the scattering length-density modulation parameters and phase	57
4.32	Hint of a 3rd order of diffraction from experimental data.	57
4.33	Plot of the maximum diffraction efficiencies predicted for the orders -1 and -2 compared with experimental data, according to the model presented in subsection 4.5.3.	58
5.1	Average total neutron counts on detector for all the collected measurement.	59
5.2	Example of spots overlap between 1st and 2nd diffraction orders.	60
5.3	Sum of measurements for tilt angle $\zeta = 77.88$ deg, with brightness and contrast enhanced.	60
5.4	Fit results for $\zeta = 77.88$, according to the model presented in subsec. 4.5.1	61
5.5	Fit results for $\zeta = 76.76$ deg, according to the model presented in subsec. 4.5.2.	62

5.6	Fit results for $\zeta = 76.76$ deg, according to the model presented in subsec. 4.5.3.	62
5.7	Experimental observation of Pendellösung interference with values predicted by the fit results	63

Chapter 1

Introduction

Holographic gratings have been used for decades in different fields such as acousto-optics, integrated optics, holography, and spectroscopy [1]. Photosensitive materials in combination with holographic techniques can be used to produce diffraction gratings for neutron- and laser- optics. In particular, nanoparticle-polymer composite (NPC) gratings have the decisive advantage of being highly versatile due to the range of possible choices of material composition, which allows the selection of the most suitable value of the coherent scattering length/absorption cross section for a specific application in neutron optics [6]. For example, with the right choice of production parameters and experimental set-up holographic gratings can be used as mirrors and beam splitters allowing to build neutron interferometers with no other optical component needed [7].

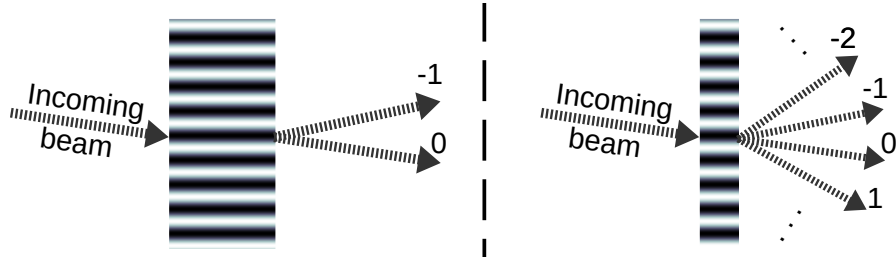


Figure 1.1: *Example of diffraction experiment in the Bragg regime (left, optically thick grating) and outside the Bragg regime (right, optically grating).*

A holographic grating with a sinusoidal modulation of the refractive index as in figure 1.1 will generate different outcomes in a diffraction experiment based on its thickness and modulation. Bragg regime gratings, also known as optically thick gratings [3], predominantly produce only two orders of diffracted waves (0th and 1st order) and the relative diffraction efficiencies

are well described by two-coupled-waves theories as the first-order theory proposed by Kogelnik [8] and the improved version including the "Beta Value Method" (BVM) proposed by Uchida [9]. They offer an effective and mathematically simple approach to analyze rocking curves from experiments in the Bragg regime [10]. However, outside of the Bragg regime their accuracy starts to decrease as optically thinner gratings generate higher orders of diffraction that are not neglectable anymore as shown in figure 1.1, and therefore a different model is needed.

Studying holographic gratings in the multi-wave regime is not only advantageous because of the possible applications as an optical component, diffraction experiments are fundamental for the investigation of the internal structure of matter. In a standard diffraction experiment with periodic structures, by measuring the intensities of diffracted signals, only the amplitude of the Fourier components can be retrieved whereas the relative phases are lost. Gratings with a near-sinusoidal modulation of the index of refraction offer simple periodic structures which can be studied to examine the effect of single Fourier components of the modulation and their relative phases [11].

The aforementioned two-coupled-waves theories have been proven to be approximations of a more comprehensive model called "Rigorous Coupled Wave Analysis (RCWA)", presented by M. G. Moharam and T. K. Gaylord [1], which does not disregard second derivatives and includes higher diffracted waves, and covers nearly the entire scope of relevant cases [12]. Despite being very accurate in its predictions, RCWA has the disadvantage of being mathematically more complex and numerically more expensive, so it seems reasonable to look for an approximation that would still ensure sufficient accuracy. As pointed out by Moharam and Gaylord themselves [1], in the case of transmission gratings (i.e. when the forward diffracted waves are dominant compared to the reflected ones, which happens to be the case in the experiment analysed in this thesis) the inclusion of higher order waves is more important than the inclusion of second derivatives. This was also tested by Neipp et al. [4] in a comparison among Kogelnik's theory, RCWA and a multi-coupled-wave theory: the last one included higher orders of diffracted waves but disregarded the second derivatives and showed high accuracy in the results with various grating types.

In this thesis, the same multi-coupled-wave theory will be applied to a data set from a neutron diffraction experiment collected between 2012 and 2013 at the Institute Laue-Langevin (ILL) [5] in Grenoble, France. The experiment was performed using an NPC grating with a nearly sinusoidal modulation of the refractive index. An attempt of analysis has been performed using two-coupled-waves theories which, however, did not yield acceptable results. The measurements clearly show the presence of non-neglectable higher

orders of diffracted waves and therefore an analysis using a multi-coupled-wave approach has been carried out within the frame of this thesis. The procedure and its result are presented in the subsequent chapters.

Chapter 2

Theory

2.1 Rigorous Coupled Wave Theory for neutrons

The following section is a re-adaptation and approximation of the Rigorous Coupled Wave Theory presented by M. G. Moharam and T. K. Gaylord [1].

2.1.1 Diffraction gratings with perfectly sinusoidal modulation of the refractive index

The refractive index for neutrons can be expressed [13] as:

$$n = \sqrt{1 - \frac{\lambda^2}{\pi} b_c \rho} \approx 1 - \frac{\lambda^2}{2\pi} b_c \rho \quad (2.1)$$

where $\lambda = h/p$ is the De Broglie wavelength of the neutron, b_c is the coherent scattering length and ρ is the number density of the medium. The modulation of the refractive index in the NPC gratings can be achieved by appropriately selecting the scattering length and/or the density of the components involved, so the scattering length-density modulation parameter is usually referred to as $b_c \Delta \rho$ (see [10, 14], for instance).

For a sinusoidal modulation as the one shown in figure 2.1 we have

$$b_c \rho(\vec{r}) = b_c \rho_0 + b_c \Delta \rho \cos(\vec{G} \cdot \vec{r}) \quad (2.2)$$

with $\vec{G} = G\hat{x} = 2\pi/\Lambda \hat{x}$, where $(\hat{x}, \hat{y}, \hat{z})$ are the unit basis vectors. Consequently, the profile of the refractive index can be expressed as

$$n(\vec{r}) \approx 1 - \frac{\lambda^2}{2\pi} b_c \rho_0 + \frac{\lambda^2}{2\pi} b_c \Delta \rho \cos(\vec{G} \cdot \vec{r}) = n_0 + \Delta n_1 \cos(\vec{G} \cdot \vec{r}) \quad (2.3)$$

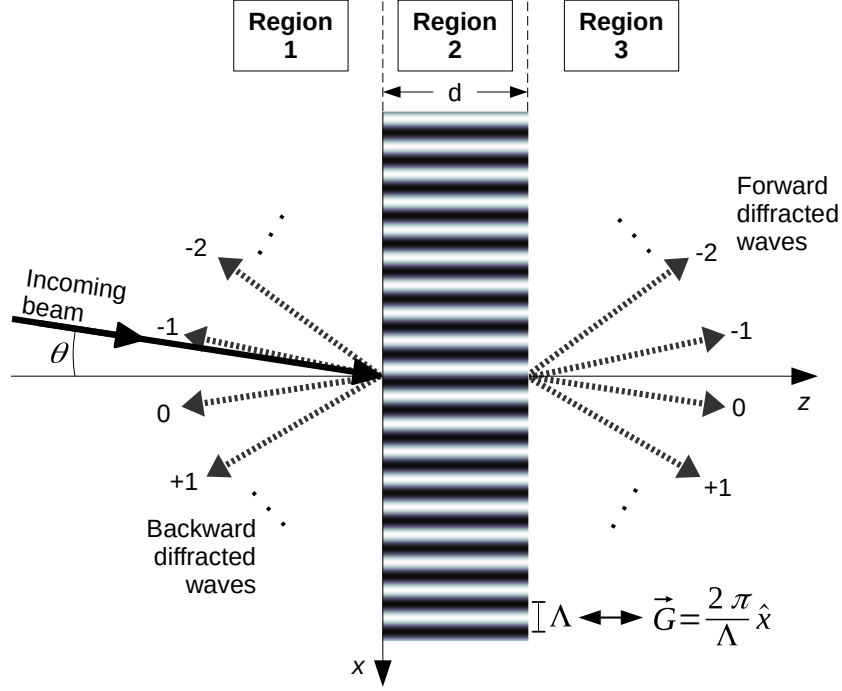


Figure 2.1: *Diffraction scheme.*

We can assume that all the wave-vectors lie on the plane (x,z) with no y-component and divide the space in three regions:

- **Region 1:** $z < 0$
- **Region 2:** $0 < z < d$
- **Region 3:** $z > d$

with $z = 0$ being the position of the entrance surface of the grating and $z = d$ the position of the exit surface; the index of refraction for the first and the third regions are taken to be equal to unity.

The wave field relative to each region can be expressed as infinite sum of waves. In the first region, the incoming beam and the backward diffracted waves are present so the wave function can be written as

$$\psi_1 = e^{-i\vec{k}_{in} \cdot \vec{r}} + \sum_j R_j e^{-i\vec{k}_{1,j} \cdot \vec{r}} \quad (2.4)$$

where $|\vec{k}_{in}| = 2\pi/\lambda = \beta$ is the norm of the incoming wave-vector in free space and R_j is the normalized amplitude of the backward diffracted wave

of vector $\vec{k}_{1,j}$ which is produced both by diffraction from within the grating volume and by boundary effects at $z = 0$ and $z = d$ [15]. In the third region we will have the transmitted, or forward diffracted, waves:

$$\psi_3 = \sum_j T_j e^{-i\vec{k}_{3,j} \cdot \vec{r}} \quad (2.5)$$

In the second region, we can express the wave function as a sum of coupled waves propagating in the diffraction grating

$$\psi_2 = \sum_j S_j(z) e^{-i\vec{k}_{2,j} \cdot \vec{r}} \quad (2.6)$$

The amplitudes $S_j(z)$ can be derived by solving the time-independent wave equation

$$\nabla^2 \psi_2 + k^2 \psi_2 = 0 \quad (2.7)$$

and to simplify the notation from now on the wave-vectors $\vec{k}_{2,j}$ of region 2 will be simply referred to as to \vec{k}_j with components $\vec{k}_{j,x}\hat{x}$ and $\vec{k}_{j,z}\hat{z}$. Let us start by calculating $\nabla^2 \psi$:

$$\frac{\partial^2}{\partial x^2} \psi = \sum_j -k_{j,x}^2 S_j(z) e^{-i\vec{k}_j \cdot \vec{r}} \quad (2.8)$$

$$\begin{aligned} \frac{\partial^2}{\partial z^2} \psi &= \frac{\partial}{\partial z} \sum_j e^{-i\vec{k}_j \cdot \vec{r}} (S'_j(z) - ik_{j,z} S_j(z)) = \\ &= \sum_j e^{-i\vec{k}_j \cdot \vec{r}} \left(\frac{\partial^2}{\partial z^2} S_j(z) - 2ik_{j,z} \frac{\partial}{\partial z} S_j(z) - k_{j,z}^2 S_j(z) \right) \end{aligned} \quad (2.9)$$

$$\nabla^2 \psi = \sum_j e^{-i\vec{k}_j \cdot \vec{r}} \left(\frac{\partial^2}{\partial z^2} S_j(z) - 2ik_{j,z} \frac{\partial}{\partial z} S_j(z) - \underbrace{(k_{j,x}^2 + k_{j,z}^2)}_{k_j^2} S_j(z) \right) \quad (2.10)$$

Before calculating the second term of equation 2.7 it is possible to make some useful approximations exploiting the fact that in the case of neutron diffraction generally $n_0 \approx 1$ and $\Delta n_1 \ll n_0$ [10]:

$$\begin{aligned} k^2 &= \beta^2 n(x)^2 = \beta^2 (n_0^2 + 2n_0 \Delta n_1 \cos(\vec{G} \cdot \vec{r}) + \Delta n_1^2 \cos^2(\vec{G} \cdot \vec{r})) \approx \\ &\approx \beta^2 + 2\beta^2 \Delta n_1 \cos(\vec{G} \cdot \vec{r}) \end{aligned} \quad (2.11)$$

so $k^2\psi$ takes the form

$$\begin{aligned}
 k^2\psi &= \beta^2 \sum_j S_j(z) e^{-i\vec{k}_j \cdot \vec{r}} + 2\beta^2 \Delta n_1 \cos(\vec{G} \cdot \vec{r}) \sum_j S_j(z) e^{-i\vec{k}_j \cdot \vec{r}} = \\
 &= \beta^2 \sum_j S_j(z) e^{-i\vec{k}_j \cdot \vec{r}} + \beta^2 \Delta n_1 (e^{i\vec{G} \cdot \vec{r}} + e^{-i\vec{G} \cdot \vec{r}}) \sum_j S_j(z) e^{-i\vec{k}_j \cdot \vec{r}} = \\
 &= \beta^2 \sum_j S_j(z) e^{-i\vec{k}_j \cdot \vec{r}} + \beta^2 \Delta n_1 \sum_j S_j(z) \left(e^{-i(\vec{k}_j - \vec{G}) \cdot \vec{r}} + e^{-i(\vec{k}_j + \vec{G}) \cdot \vec{r}} \right)
 \end{aligned} \tag{2.12}$$

The Floquet theorem restricts the possible fields that can exist in a periodic structure. In our case, the periodicity only extends in the x direction so the following condition is imposed

$$\vec{k}_j \cdot \hat{x} = \vec{k}_0 \cdot \hat{x} + j\vec{G} \cdot \hat{x} \tag{2.13}$$

where

$$|\vec{k}_0| = \beta n_0 \approx \beta \tag{2.14}$$

A common choice for the coupled wave-vectors, also adopted in the original treatment of the RCWA [1, 15], is

$$\vec{k}_j = \vec{k}_0 + j\vec{G} \tag{2.15}$$

However, equation 2.15 is only one of the possibilities as any set of coupled wave-vectors respecting equation 2.13 is a valid choice [16].

It has been shown that when working with first order approximations equation 2.15 fails to predict the shape of the diffraction efficiencies already in the two-waves case, while better results are achieved by choosing [16, 9, 12]

$$|\vec{k}_j| = |\vec{k}_0| \approx \beta \tag{2.16}$$

in combination with equation 2.13. In the two-wave case this choice of initial conditions is referred to as Beta Value Method (BVM) and it has the advantage of ensuring energy conservation, in contrast to the K-Vector Closure Method (KVCM) corresponding equation 2.15 [10, 12]. For these reasons, the latter will be the preferred choice in this analysis and the field propagating in the grating takes the form shown in figure 2.2. Nevertheless, without performing any approximation both choices would lead to the same result [16]

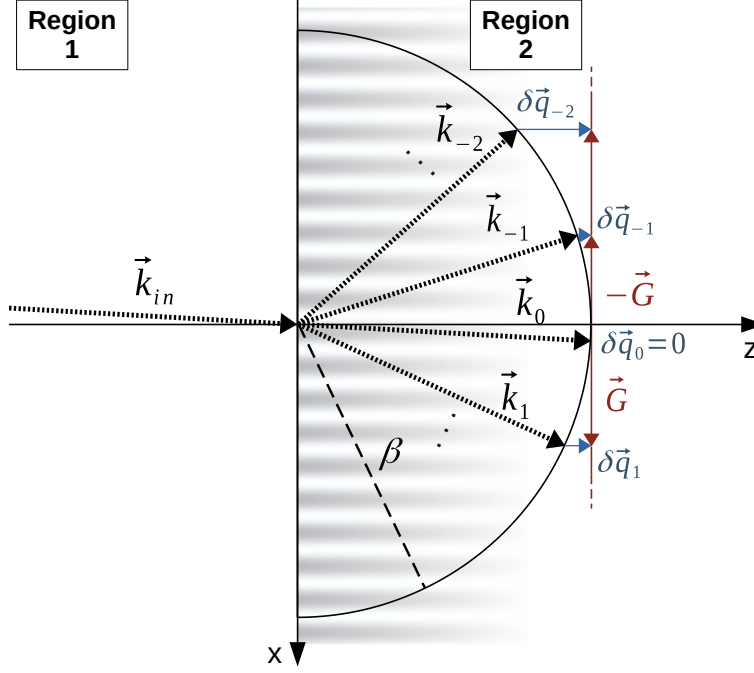


Figure 2.2: Geometry of the coupled wave-vectors. (N.B. the fading color of the diffraction grating is just to make the figure more readable, it has no physical meaning.)

The geometry of the coupled waves-vectors derived from equation 2.16 results in the following conditions:

$$\begin{cases} k_{j,x} &= \beta \sin \theta + jG \\ k_{j,z} &= \sqrt{(\beta)^2 - (k_{j,x})^2} = \beta \sqrt{1 - (\sin \theta + jG/\beta)^2} \\ \delta q_j &= \beta \cos \theta - k_{j,z} = \beta (\cos \theta - \sqrt{1 - (\sin \theta + jG/\beta)^2}) \end{cases} \quad (2.17)$$

where δq_j is sometimes referred as phase-mismatch parameter [12]. The quantities $k_{j,z}$ can be positive and real (propagating waves) or negative and imaginary (evanescent waves). Consequently, we obtain the following relations

$$\vec{k}_j - \vec{G} = \vec{k}_{j-1} + (\delta q_{j-1} - \delta q_j) \hat{z} \quad (2.18)$$

$$\vec{k}_j + \vec{G} = \vec{k}_{j+1} + (\delta q_{j+1} - \delta q_j) \hat{z} \quad (2.19)$$

and

$$\begin{aligned}
 & \beta^2 \Delta n_1 \sum_j S_j(z) \left(e^{-i(\vec{k}_j - \vec{G}) \cdot \vec{r}} + e^{-i(\vec{k}_j + \vec{G}) \cdot \vec{r}} \right) = \\
 & = \beta^2 \Delta n_1 \sum_j S_j(z) \left(e^{-i(\vec{k}_{j-1} + (\delta q_{j-1} - \delta q_j) \hat{z}) \cdot \vec{r}} + e^{-i(\vec{k}_{j+1} + (\delta q_{j+1} - \delta q_j) \hat{z}) \cdot \vec{r}} \right) = \quad (2.20) \\
 & = \beta^2 \Delta n_1 \sum_j e^{-i\vec{k}_j \cdot \vec{r}} \left(S_{j-1}(z) e^{-i(\delta q_{j-1} - \delta q_j)z} + S_{j+1}(z) e^{-i(\delta q_{j+1} - \delta q_j)z} \right)
 \end{aligned}$$

In the last step I have re-arranged the terms in the sum for convenience, an explicit example with only 5 waves is provided in appendix A.1. As a final result we get:

$$\begin{aligned}
 k^2 \psi = \sum_j e^{-i\vec{k}_j \cdot \vec{r}} \beta^2 [& S_j(z) + \Delta n_1 (S_{j-1}(z) e^{-i(\delta q_{j-1} - \delta q_j)z} + \\
 & + S_{j+1}(z) e^{-i(\delta q_{j+1} - \delta q_j)z})] \quad (2.21)
 \end{aligned}$$

By inserting equation 2.10 and 2.21 in equation 2.7, we get to the following form:

$$\begin{aligned}
 -S_j''(z) + 2ik_{j,z} S_j'(z) = & \beta^2 \Delta n_1 (S_{j-1}(z) e^{-i(\delta q_j - \delta q_{j-1})z} + \\
 & + S_{j+1}(z) e^{-i(\delta q_j - \delta q_{j+1})z}) \quad (2.22)
 \end{aligned}$$

where $\partial^2/\partial z^2 S_j(z)$ and $\partial/\partial z S_j(z)$ were indicated as $S_j''(z)$ and $S_j'(z)$ respectively. So far, no approximation has been applied except from the ones on the index of refraction.

As anticipated in the introduction, despite equation 2.22 being precise description of the problem, it is reasonable to look for an approximated version that is numerically less expensive but still ensures sufficient accuracy. Moharam and Gaylord already pointed out that in the case of transmission gratings the inclusion of higher order waves is more important than the inclusion of second derivatives, as also tested by Neipp et al. [4]. Especially in the case of neutrons we do not expect a significant variation in the envelope of the waves inside the diffraction grating so it seems appropriate to discard the second derivatives.

As a consequence of the latter approximation the number of waves that is possible to derive by solving the wave equation is reduced to half of the initial amount: the waves propagating in the grating are retained and the ones generated by boundary effects are disregarded. Discarding second derivatives and consequently the boundary conditions turns the analysis into a filled-space problem (a grating filling all space) with no actual physical boundaries

but arbitrary conditions at $z = 0$ and $z = d$ that are used only to obtain an approximate mathematical formulation of the problem [15]. Equation 2.22 takes the new form

$$2ik_{j,z}S'_j(z) = \beta^2\Delta n_1 (S_{j-1}(z)e^{-i(\delta q_j - \delta q_{j-1})z} + S_{j+1}(z)e^{-i(\delta q_j - \delta q_{j+1})z}) \quad (2.23)$$

which can be further manipulated to turn it into a more suitable form. Let us define $\tilde{S}_j = S_j e^{i\delta q_j z}$ to obtain

$$2ik_{j,z}(\tilde{S}'_j(z) - i\delta q_j \tilde{S}_j(z)) = \beta^2\Delta n_1 (\tilde{S}_{j-1}(z) + \tilde{S}_{j+1}(z)) \quad (2.24)$$

and consequently

$$2ik_{j,z}\tilde{S}'_j(z) = -2k_{j,z}\delta q_j \tilde{S}_j(z) + \beta^2\Delta n_1 (\tilde{S}_{j-1}(z) + \tilde{S}_{j+1}(z)) \quad (2.25)$$

Equation 2.25 can be expressed in an infinite-dimensional matrix form, and in order to compute it numerically only a limited number of waves can be retained. The number of coupled waves to retain is chosen based on the expected number of non-negligible waves and in the case of $2m+1$ waves the system of ODE can be written in the matrix form

$$\vec{S}'(z) = \begin{pmatrix} a_{-m} & b_{-m+1} & 0 & \dots & \dots & 0 \\ b_{-m+1} & a_{-m+1} & b_{-m+2} & 0 & \dots & \vdots \\ 0 & b_{-m+2} & a_{-m+2} & \ddots & \ddots & \vdots \\ \vdots & 0 & \ddots & \ddots & b_{m-2} & 0 \\ \vdots & \vdots & \ddots & b_{m-2} & a_{m-1} & b_{m-1} \\ 0 & \dots & \dots & 0 & b_{m-1} & a_m \end{pmatrix} \vec{S}(z) = [M] \vec{S}(z) \quad (2.26)$$

where $[M]$ is the tridiagonal matrix of the coefficients:

$$\begin{cases} a_j &= i\delta q_j \\ b_j &= -i\frac{\beta^2\Delta n_1}{2k_{j,z}} \end{cases} \quad (2.27)$$

By starting from the ansatz

$$\vec{S}(z) = \vec{A}e^{\lambda z} \quad (2.28)$$

the solution is reduced to the eigenvalues/eigenvectors problem:

$$\vec{S}'(z) = [M] \vec{S}(z) = \lambda \vec{S}(z) \quad (2.29)$$

Once the eigenvalues λ_i and the eigenvectors $\vec{A}_i e^{\lambda_i z}$ have been found, the solution can be constructed as follows

$$\vec{S}(z) = \sum_i C_i \vec{A}_i e^{\lambda_i z} \quad (2.30)$$

where C_i are coefficients to be determined by the initial conditions. In the case of an unslanted grating where the boundary conditions have been disregarded there are no backward diffracted waves, so the amplitude at $z = 0$ must correspond to

$$\vec{S}(0) = \delta_{j,0} \quad (2.31)$$

i.e. only the incident wave is present. The diffraction efficiency η_j corresponding to the j -th order can then be calculated as

$$\eta_j = |S_j(d)|^2 \quad (2.32)$$

It is worth mentioning that the presented theory can be used in any scenario in which it is reasonable to discard the second derivatives and the boundary effects, and it reduces to the two-coupled-waves theories generally used for the Bragg regime when higher orders of diffraction are discarded [1, 15].

2.1.2 Diffraction gratings presenting additional Fourier components in the modulation of the refractive index

If we want to include two (or more) Fourier components in the grating modulation such as

$$n(x) = n_0 + \Delta n_1 \cos(\vec{G} \cdot \vec{r}) + \Delta n_2 \cos(2\vec{G} \cdot \vec{r} + \phi) \quad (2.33)$$

equation 2.11 would take the following form

$$\begin{aligned} k^2 &= \beta^2 n(x)^2 = \beta^2 (n_0^2 + 2n_0 \Delta n_1 \cos(\vec{G} \cdot \vec{r}) + 2n_0 \Delta n_2 \cos(2\vec{G} \cdot \vec{r} + \phi) + \\ &\quad + 2\Delta n_1 \Delta n_2 \cos(\vec{G} \cdot \vec{r}) \cos(2\vec{G} \cdot \vec{r} + \phi) + \Delta n_1^2 \cos^2(\vec{G} \cdot \vec{r}) \Delta n_2^2 \cos^2(\vec{G} \cdot \vec{r})) \approx \\ &\approx \beta^2 + 2\beta^2 \Delta n_1 \cos(\vec{G} \cdot \vec{r}) + 2\beta^2 \Delta n_2 \cos(2\vec{G} \cdot \vec{r} + \phi) \end{aligned} \quad (2.34)$$

where again the terms of order Δn_i^2 have been neglected. With a similar process as in the previous section (equations 2.12 to 2.19), we have:

$$\vec{k}_j - 2\vec{G} = \vec{k}_{j-2} + (\delta q_{j-2} - \delta q_j) \hat{z} \quad (2.35)$$

$$\vec{k}_j + 2\vec{G} = \vec{k}_{j+2} + (\delta q_{j+2} - \delta q_j) \hat{z} \quad (2.36)$$

and consequently our differential equation will be of the form

$$2ik_{j,z}\tilde{S}'_j(z) = -2k_{j,z}\delta q_j\tilde{S}_j(z) + \beta^2\Delta n_1 \left(\tilde{S}_{j-1}(z) + \tilde{S}_{j+1}(z) \right) + \beta^2\Delta n_2 \left(e^{-i\phi}\tilde{S}_{j-2}(z) + e^{+i\phi}\tilde{S}_{j+2}(z) \right) \quad (2.37)$$

This will add to the matrix in equation 2.26 two extra diagonals of terms c_j^\pm :

$$\vec{S}'(z) = \begin{pmatrix} a_{-m} & b_{-m+1} & c_{-m+2}^+ & 0 & \dots & 0 \\ b_{-m+1} & a_{-m+1} & b_{-m+2} & \ddots & \ddots & \vdots \\ c_{-m+2}^- & b_{-m+2} & a_{-m+2} & \ddots & \ddots & \ddots \\ 0 & \ddots & \ddots & \ddots & b_{m-2} & c_{m-2}^+ \\ \vdots & \vdots & \ddots & b_{m-2} & a_{m-1} & b_{m-1} \\ 0 & \dots & \dots & c_{m-2}^- & b_{m-1} & a_m \end{pmatrix} \vec{S}(z) = [M] \vec{S}(z) \quad (2.38)$$

where

$$\begin{cases} a_j &= i\delta q_j \\ b_j &= -i\frac{\beta^2 n_0 \Delta n_1}{2k_{j,z}} \\ c_j^\pm &= -i\frac{\beta^2 n_0 \Delta n_2}{2k_{j,z}} e^{\pm i\phi} \end{cases} \quad (2.39)$$

The solution can be found in the same way as in the previous section and a similar procedure can be used to add even more Fourier components to equation 2.33.

2.1.3 Pendellösung interference

As the coupled waves propagate inside the diffraction grating, they interfere with each other causing a spatial modulation of their amplitudes: this phenomena is known as Pendellösung (in English: pendulum solution) interference. The name was given by P.P. Ewald because, in the dynamical diffraction theory (DDT) for X rays, this interference causes a beating of the amplitudes between the 0th and the 1st order of diffraction which resembles the transfer of energy between two weakly coupled pendulums [17]. The DDT is also valid for neutrons and it was demonstrated to be equivalent to the RCWA [10, 1, 15]. The Pendellösung interference was observed for neutrons by Shull [18], where a coherent transfer of neutron flux between the 0th and 1st order of diffraction was observed [13].

For fixed values of incoming wavelength λ , incident angle θ and grating modulation profile, the Pendellösung interference results in a beating of the coupled waves amplitudes along the thickness of the grating [13]. In a diffraction configuration as the one shown in figure 2.1 the effective thickness of a diffraction grating can be increased by tilting of an angle ζ around an axes parallel to the x direction, as shown in figure 2.3.

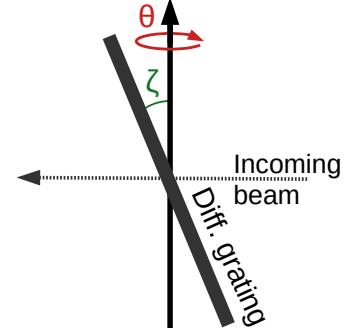


Figure 2.3: Example of thickness modulation by tilt

Being able to control the thickness of the grating allows to use the Pendellösung interference to modulate the amplitudes of the diffraction efficiencies, broadening the field of possible applications as an optical component. For example, with the right choice of angles θ and ζ , a beam splitter configuration, a mirror-like configuration or a transmission configuration can be realized as shown in figure 2.4. A test of the mirror-like configuration was realized by Klepp et al. [14] reaching a reflectivity of 0.9, while a neutron interferometer was realized by Pruner et al. [7] using three holographic gratings in succession.

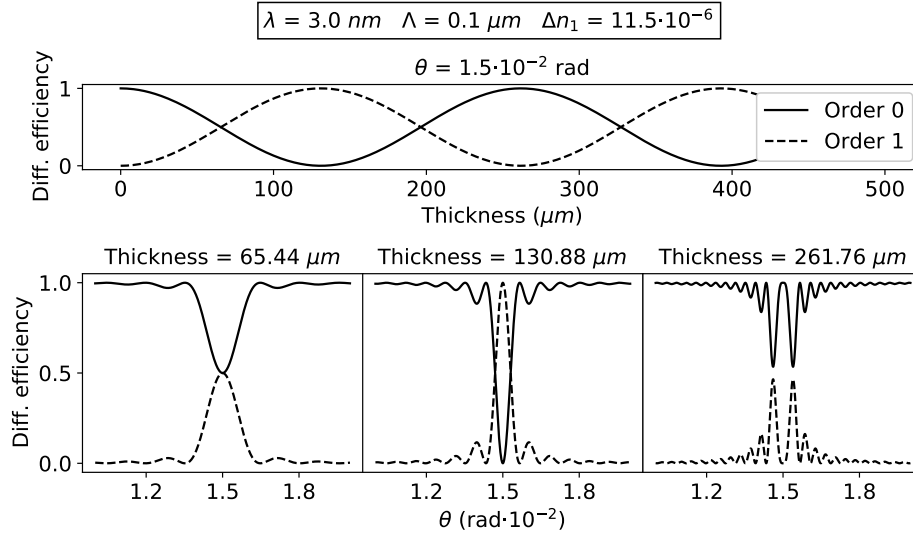


Figure 2.4: Numerical simulations of the Pendellösung interference for different thicknesses (top) and three possible configurations (bottom): 50:50 beam splitter (left), mirror-like (center) and transmission (right).

In the case of a configuration in which the +1 and -1 diffraction orders are present for the same value of θ , with the right choice of parameters one

could create a three-port $(-1,0,1)$ beam splitter as shown in figure 2.5. This was experimentally realised by Klepp et al. [19].

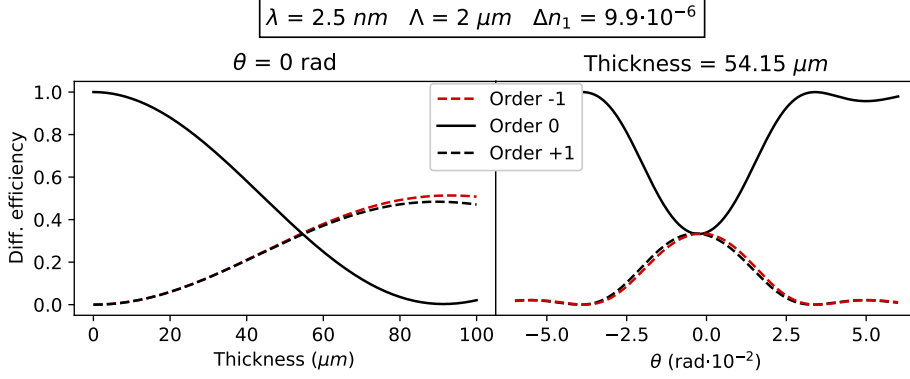


Figure 2.5: Numerical simulation of a three-port beam splitter configuration.

When working in the multi-wave regime the Pendellösung interference can be potentially used to modulate the amplitudes of diffraction orders higher than the first. Figure 2.6 shows numerical simulations of a monochromatic beam of neutron of $\lambda = 3$ nm going through a diffraction grating of profile

$$n(x) = n_0 + \Delta n_1 \cos(\vec{G} \cdot \vec{r}) + \Delta n_2 \cos(2\vec{G} \cdot \vec{r} + \phi) \quad (2.40)$$

with modulation period $\Lambda = 0.5$ μm at a fixed incident angle $\theta = 0.0055$. The plots show three different setting of the modulation amplitudes Δn_1 and Δn_2 with the relative phase ϕ .

Modelling the Pendellösung interference is also useful as an investigation method for small angle variations of the incident beam [20]. In the cases treated until now, the incident beam does not have any component along the y axis so the tilt angle ζ is only due to the inclination of the sample. Let us now consider the case in which the sample is kept at a fixed position ζ_0 and the beam is tilted of an angle $\Delta\zeta$. The thickness experienced by the beam can be calculated as

$$d = \frac{d_0}{\cos(\zeta_0 + \Delta\zeta)} \quad (2.41)$$

with d_0 being the original thickness of the sample and $\zeta = \zeta_0 + \Delta\zeta$.

When approaching $\zeta = 90^\circ$ the diffraction efficiency curves start to oscillate very steeply as shown in figure 2.7 and, in principle, with an appropriate choice of the angle ζ_0 then is possible to adjust the accuracy of a measurement of a tilt of the beam.

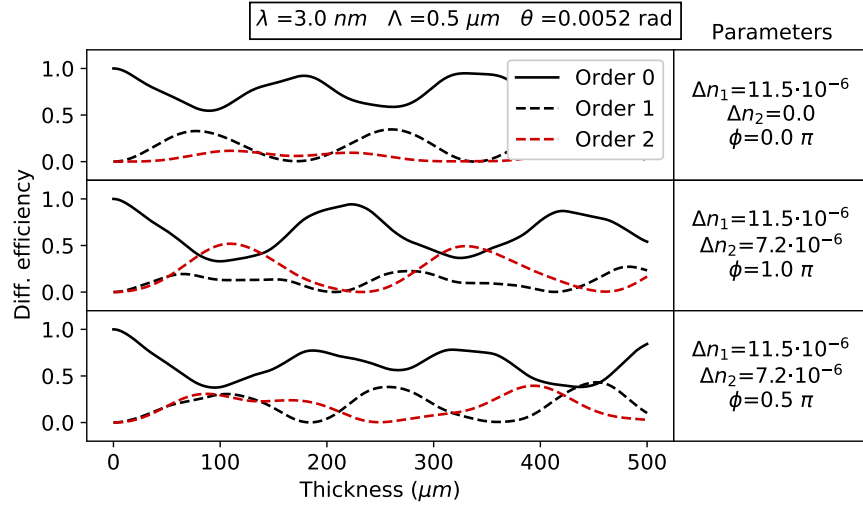


Figure 2.6: Numerical simulation of Pendellösung interference for 0th, 1st, and 2nd order of diffraction.

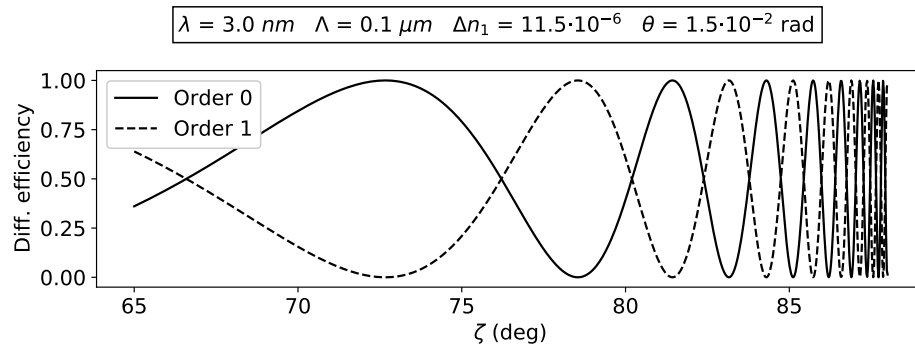


Figure 2.7: Pendellösung interference for different tilt angles ζ

Chapter 3

The experiment

3.1 The sample

The sample was a nanoparticle-polymer composite (NPC) diffraction grating of thickness $\sim 78 \mu\text{m}$ with a near-sinusoidal modulation of the refractive index with period $\Lambda = 0.5 \mu\text{m}$. The modulation was generated by illuminating a mixture of SiO_2 nanoparticles and monomers with light of sinusoidal intensity obtained from the interference setup as represented in figure 3.1. The

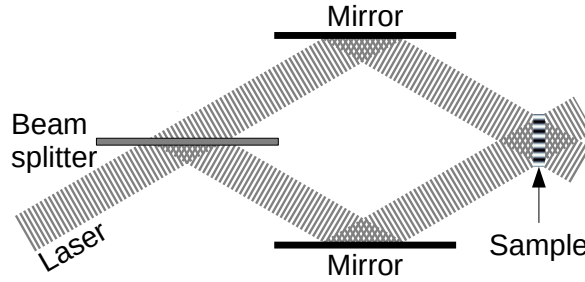


Figure 3.1: *Interference setup used to obtain light of sinusoidal intensity profile at the sample position.*

light induces the photopolymerization of the monomers which causes their accumulation in the brighter areas. As a consequence, the photoinsensitive inorganic nanoparticles experience counterdiffusion from the bright areas to the dark regions [21] shown in figure 3.2. Due to the non-linearity of the diffusion processes the recorded modulation of the refraction index will most likely include low-amplitude higher Fourier components.

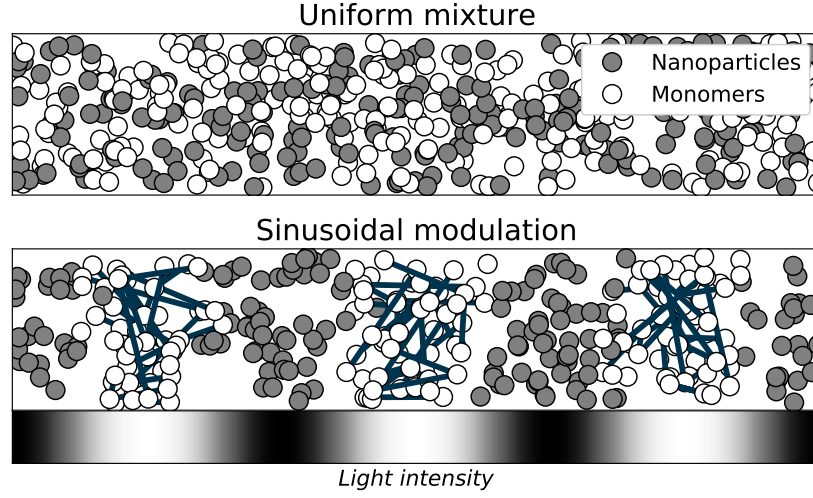


Figure 3.2: Mixture of nanoparticles and monomers before (top) and after (bottom) light-induced hologram recording.

3.2 The measurements

Let us consider a diffraction grating with a periodic modulation of the refractive index and an incident beam of wavelength λ . A rotation of the grating

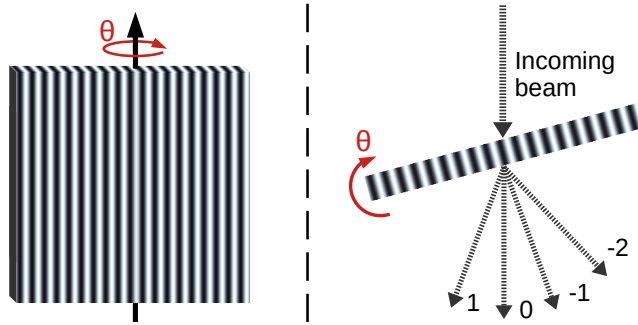


Figure 3.3: Diffraction grating with sinusoidal modulation of the refractive index.

performed as shown in figure 3.3 will generate diffracted waves of different intensities for some values of the angle of incident: the experiment consisted in measuring the intensities of the different orders of diffraction generated by a collimated neutron beam passing through the diffraction grating on step-wise variation of the incident angle θ .

As previously mentioned, allowing rotations around an additional orthogonal axis ζ as shown in figure 3.4 offers the possibility of increasing the ef-

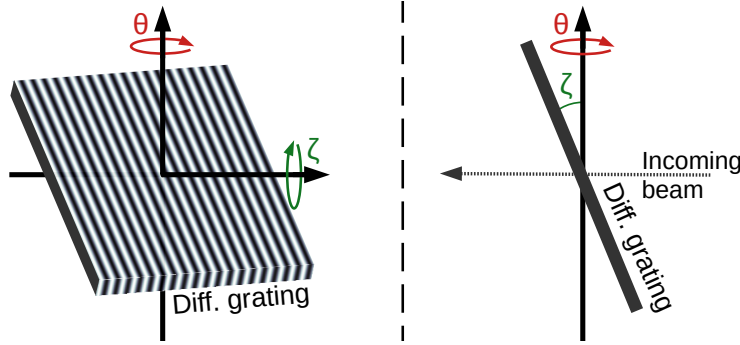


Figure 3.4: *Modulation of the thickness of the diffraction grating by tilting.*

fective thickness of the sample as

$$d = \frac{d_0}{\cos \zeta} \quad (3.1)$$

with d_0 being the original thickness, and in this way the Pendellösung effect can be used to modulate the intensities of the diffracted waves [6].

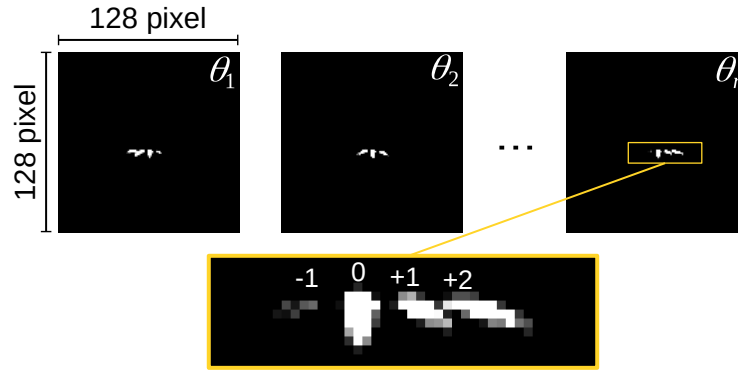


Figure 3.5: *Example of images from the measurement (contrast enhanced).*

In each measurement session the tilt angle ζ is kept fixed and data for a range of different values of θ are collected. The detector registers the neutron counts for each of the 128x128 pixels in a defined time interval, i.e. exposure time, and exports the data as a text file, which can successively be turned into pictures if needed as shown in figure 3.5. Successively, the neutron counts in each diffraction spot are assigned to the different orders of diffraction for each value of the incident angle as shown in figure 3.6. A more detailed description of the procedure will be given in section 4.2.

Exposure time, number of measurements and angular resolution of the steps along θ are set independently for each session. In total 13 sessions have

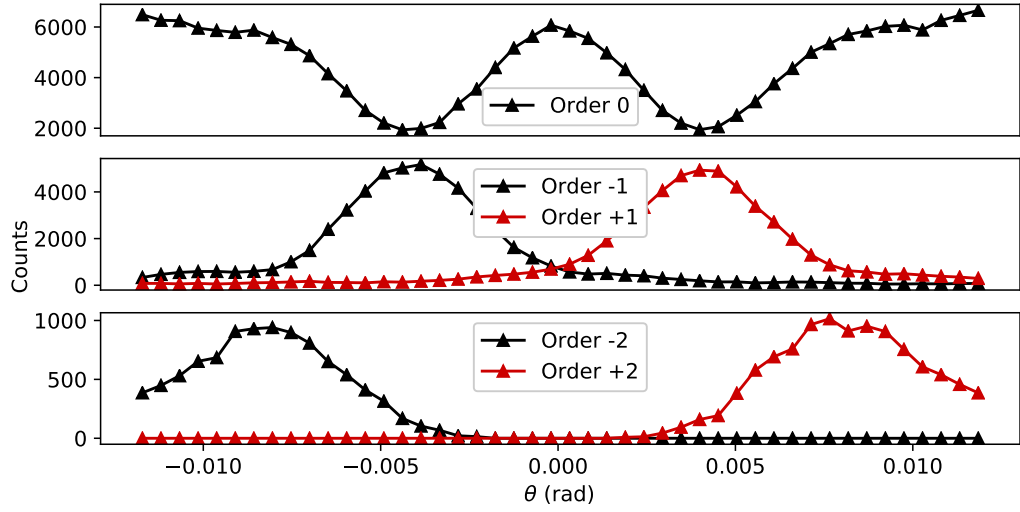


Figure 3.6: *Example the neutron counts in each diffraction spot assigned to the different diffraction orders for step-wise variation of θ*

been selected for the analysis and a summary of the experimental settings is shown in table 3.1 below.

Tilt angle ζ (deg)	Number of θ -values	Step-width (deg)	Exposure time per step (hours)
0	26	0.03	1
40	46	0.03	1
48	28	0.05	1.5
61	18	0.05	1
69	16	0.05	1
71	20	0.03	1
74.52	28	0.03	1
75.64	60	0.03	1
76.76	43	0.03	1.5
77.88	51	0.03	1
79	21	0.03	1
80	20	0.03	1
81	19	0.03	1

Table 3.1: *Summary of the measurement sessions to be analysed.*

3.3 Experimental set-up

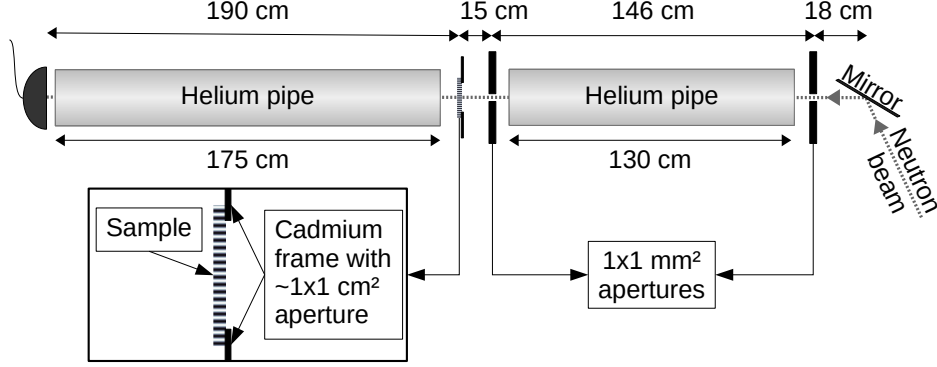


Figure 3.7: *Top view of the diffraction plane.*

A scheme of the experimental set-up is shown in figure 3.7. The space in front of the first beam aperture was limited by the room dimensions, so a mirror was placed in front of the aperture in order to gain length. After the mirror two square-collimating slits of size $1 \times 1 \text{ mm}^2$ have been placed at a distance of 146 cm between each other, just by geometrical considerations this should reduce the beam divergence half-angle to a value of approximately $\Delta\theta \approx 0.00068 \text{ rad}$ both horizontally and vertically. Additionally, a Cadmium frame was attached to the sample in order to limit the area of interaction to the illuminated part. Two pipes filled with Helium (steady flow) have been used to reduce neutron-air scattering along the set-up and a neutron detector of 128×128 pixels with pixel size corresponding to $2 \times 2 \text{ mm}^2$ was placed at a distance of 190 cm from the sample.

3.4 The instrument

The experiment was performed at the instrument PF2 of the Institute Laue-Langevin, Grenoble, France [5]. The neutron source provided a beam of very cold neutrons (VCN), which can be approximately defined as a range of wavelengths between cold neutrons ($\lesssim 1 \text{ nm}$) and ultra cold neutrons ($\gtrsim 50 \text{ nm}$) [22].

A measurement of the wavelength distribution was carried out by Blackner et al. [23] and it presented an asymmetric profile with a peak at around $\lambda_{max} = 3.7 \text{ nm}$ and a relative width of $\Delta\lambda/\lambda_{mean} \approx 0.3$, where $\Delta\lambda$ corresponds to the full-width half-maximum, as shown in figure 3.8. The steep slope in the direction of shorter wavelengths can be attributed to the usage

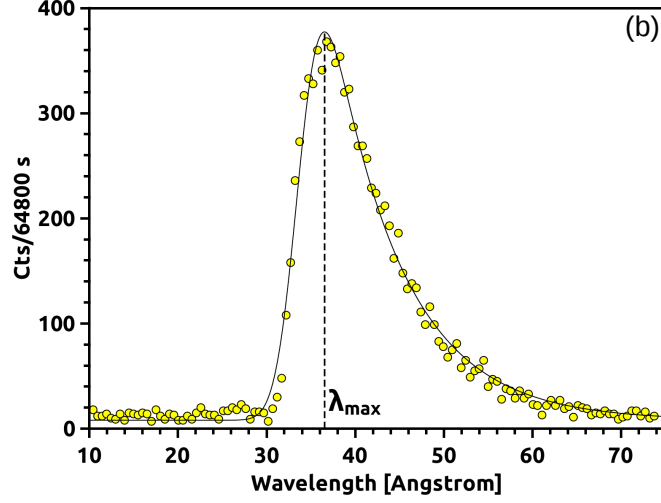


Figure 3.8: *Measured wavelength distribution by Blaickner et al. fitted by an exponentially modified Gaussian (EMG) [23].*

of a mirror to re-direct the beam as shown in figure 3.7. In figure 3.8 it is also possible to see that the distribution can be accurately represented by an exponentially modified Gaussian (EMG) distribution:

$$\rho(\lambda) = \frac{1}{2\tau} \exp\left(\frac{2\mu + \sigma^2/\tau - 2\lambda}{2\tau}\right) \operatorname{erf}\left(\frac{\mu + \sigma^2/\tau - \lambda}{\sqrt{2}\sigma}\right) \quad (3.2)$$

Knowing the wavelength distribution is fundamental to determine the outcome of a diffraction experiment because, as shown in chapter 2.1, the diffraction efficiencies depend on λ . The aforementioned measurement of the distribution was performed only selecting a fraction of the beam around the spot with higher intensity which does not represent the overall wavelength distribution. A measurement performed by Oda et al. in 2017 [24] at the same facility but on a wider section of the neutron beam showed that the wavelength distribution changes depending on the selected area, so we do not expect necessarily to always find the same distribution for different set-up configurations.

Chapter 4

Data analysis and discussion

4.1 Preliminary analysis

In order to have a general overview of the measurements, all the data collected by the 128x128 pixel detector have been turned to 32bit gray-scale pictures as shown in figure 4.1 The software Fiji-ImageJ [25] has been used for a preliminary and more visual approach to the analysis.

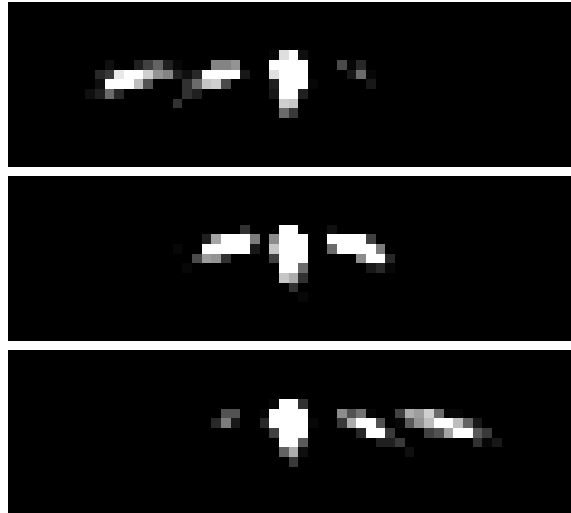


Figure 4.1: *Example of three measurements for different values of θ in 32-bit grey-scale format (cropped and with contrast enhanced.)*

4.1.1 Shape, size and position of the spots

The first thing we can notice from figure 4.1 is that the spots exhibit an elongated shape: neutrons with longer wavelengths end up at lower points on the detector because of gravitational deflection of the beam. For instance, neutrons of 4 nm wavelength exiting the source with a purely horizontal velocity of about 100 m/s experience a vertical deflection of 4 mm for a 3 m horizontal flight distance. This assumption is also in agreement with the fact that the diffracted spots increase in distance from the 0th order as we move downward since the Bragg angle increases with the wavelength.

A measurement in off-Bragg position, i.e. at an incident angle such that only the transmitted beam is present with no diffracted waves, has been used to check the horizontal profile of the neutron beam, the average width of the spot seems to have a Gaussian profile of $\sigma \approx 1.24 \text{ mm}$ as shown in figure 4.2. The width of the fitted Gaussian can be used as an indication of the beam collimation: by using the length of $2\sigma \approx 2.48 \text{ mm}$ we get an estimated divergence half-angle of $\Delta\theta \approx 0.00071 \text{ rad}$, which is in agreement with the value of $\Delta\theta \approx 0.00068 \text{ rad}$ expected simply based on the geometry of the experimental set-up.

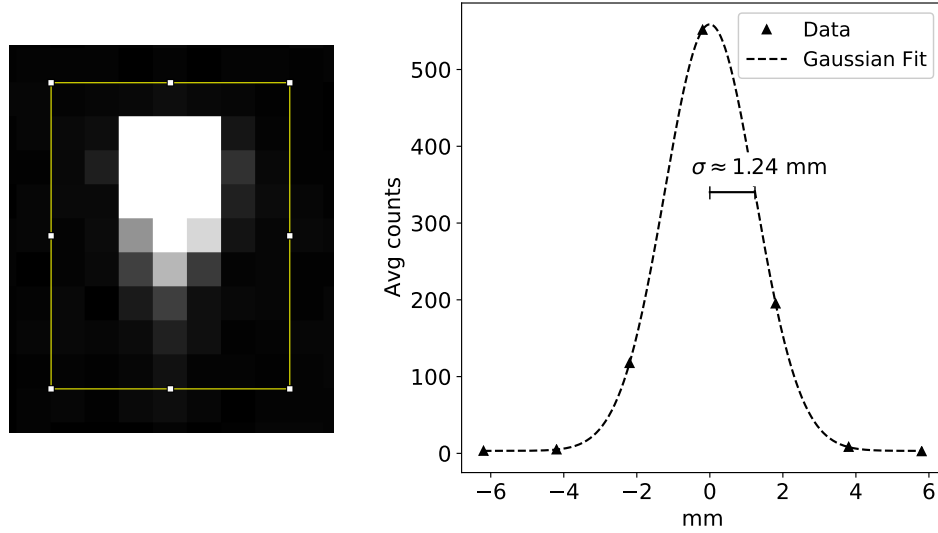


Figure 4.2: *Plot of the average horizontal profile of the spot in the sample-less measurement.*

By comparing shapes and positions of the spots for different tilt angles ζ two main observations can be made:

- as shown in figure 4.3 we can see that the vertical length of the spot tends to get shorter with higher tilt angles. This is probably due to the experimental set-up: as the sample gets tilted the cadmium frame placed on the grating gets in the way of the neutron beam;
- the spots are not always found in the same place on the detector: between measurement sessions the set-up has been modified;

Selecting different parts of the neutron beam will inevitably affect the wavelength distribution [24], so any change in the size, shape and/or position of the spots has to be taken into account.

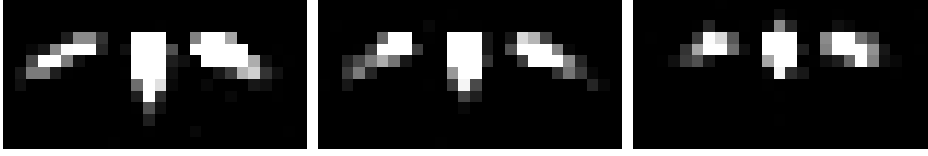


Figure 4.3: *Diffraction spots for three different tilt angles: $\zeta = 0^\circ$ (left), $\zeta = 69^\circ$ (center), and $\zeta = 80^\circ$ (right) (cropped and with contrast enhanced).*

During the experimental campaign, the set-up has been changed two times, once intentionally and once unintentionally. The measurement sessions mentioned in table 3.1 are not ordered chronologically. The first that was performed was $\zeta = 40$ deg and after this session the arrangement of the grating was changed because part of the supporting structure was getting in the way for higher tilt angles, preventing the beam from going through the sample. Successively at the end of session $\zeta = 74.52$ deg for an unknown reason the position of the diffracted spots is shifted of about 2-3 pixels to the left, and seems to stay there for all the successive measurements. Table 4.1 shows the measurement sessions grouped by same set-up and position on the detector. This is useful to compare possible similarities in wavelength distribution among groups.

Group 1	Group 2	Group 3
40 deg	74.52 deg	0 deg
	75.64 deg	48 deg
	76.76 deg	61 deg
	77.88 deg	69 deg
	79 deg	71 deg
	80 deg	
	81 deg	

Table 4.1: *Measurement sessions divided based on the set-up changes.*

4.1.2 Diffracted spots

An issue that arises by going through the measurements is that the 1st and the 2nd order of diffraction spots overlap for some values of θ as shown in figure 4.4. This is probably due to the wide wavelength distribution that causes the second diffraction order of the shorter wavelengths to appear in the same θ -range of the first order of the longer wavelengths.

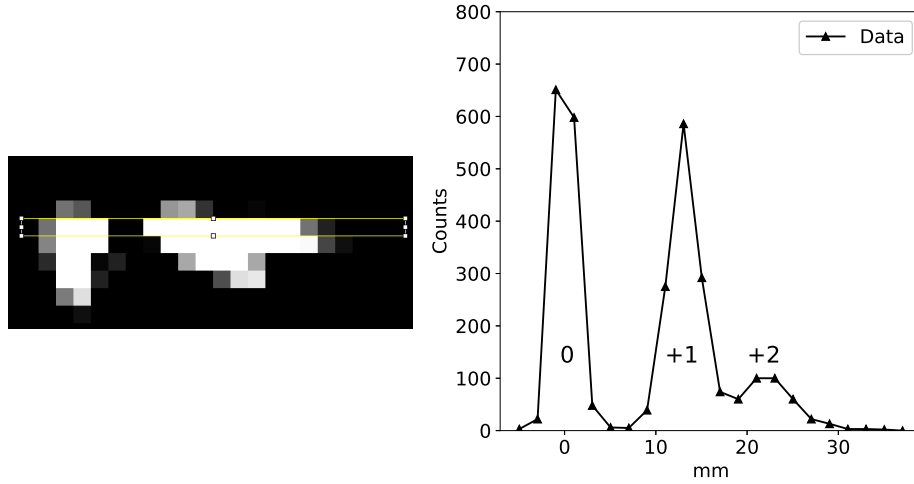


Figure 4.4: *Example of spots overlap between 1st and 2nd diffraction orders for $\zeta = 40$ deg (left), with plot of the neutron counts profile (right).*

When calculating the diffraction spots intensities the neutron counts have to be distributed among the different orders of diffraction. The latter requires a solution to address the overlap region. The method is presented more in detail in section 4.2.

4.1.3 Neutron intensity

Different factors might affect the average neutron intensity in a measurement. Some of them depend on adjustable parameters such as the exposure time or the collimation set-up, others on statistical factors as the nuclear process producing the neutrons. Even if it is not expected to measure a perfectly constant intensity among different measurements, sudden and significant changes in the total average neutron counts during the same measurement sessions might be an indication of compromised data.

Figure 4.5 shows the total average neutron counts for each measurement that has been taken, not normalized by exposure time. Some data points in this plot (marked by arrows) present a considerable dip in intensity

which might be due to several reasons: temporary changes in the neutron source, temporary changes in the neutron flux, or intentional interruption by people operating in the same facility; these data will be discarded in the analysis.

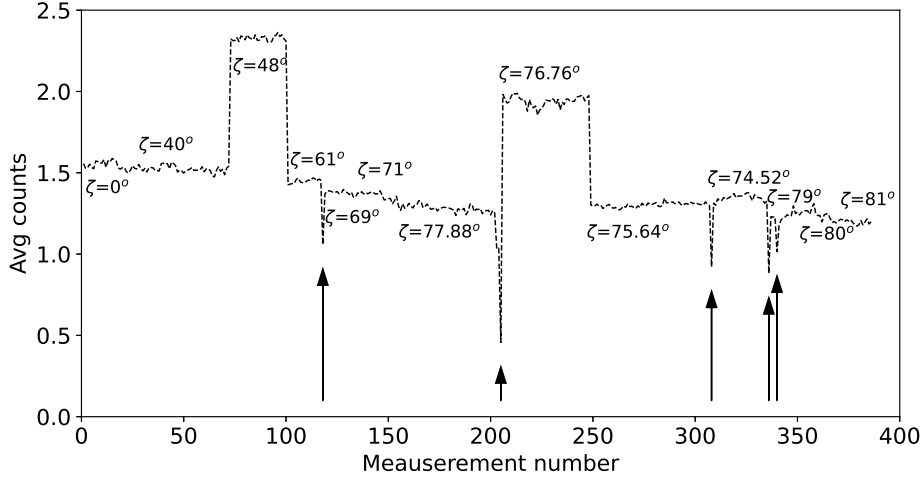


Figure 4.5: Average neutron counts for all the collected measurement

Moreover, by summing all the pictures in a measurement session and enhancing brightness and contrast as shown in figure 4.6, it is possible to see a shadow cast by the helium pipes used to reduce neutron-air scattering. The bright spots over the bottom part of the shadow are due to neutrons bouncing off the pipe. It is difficult to infer the position of the pipe based on the shadow and if it is interfering partially with the beam and the diffracted waves (increasing local background or cutting-off diffraction spots), but this possibility can not be rejected based on the information available.

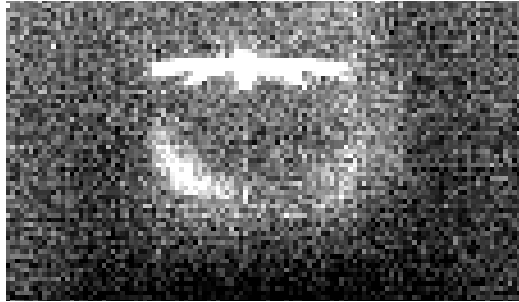


Figure 4.6: Sum of measurements for tilt angle $\zeta = 77.88$ deg, with brightness and contrast enhanced.

4.2 Diffraction efficiencies

In order to apply the theory presented in chapter 2.1, it is necessary to extract the values of the diffraction efficiencies from the measurements. The following part of the data analysis has been carried out using Spyder (version 4.1.4) [26], a free and open source scientific environment for the programming language Python (version 3.8) [27].

4.2.1 Definition of the region of interest

The first step is to define the region of interest (ROI) of each measurement, i.e. the pixel region in which all the diffraction spots are present.

Let us consider a single measurement session for a fixed tilt angle ζ , consisting of n measurements along θ . An algorithm can be developed to find the first row of the ROI as follows:

1. **Import the measurements as 2D arrays and stack them in a 3D array.**

Each measurement for a specific angle θ_z is previously organized in a 2D array in which the x and y axes represent the horizontal and vertical direction of the detector respectively. The 2D arrays are then stacked in a 3D array in which the z axis represents the different angles θ_z as shown in figure 4.7. In this way, the array element of coordinates $[x, y, z]$ will identify the neutron counts measured on a pixel of position (x, y) on the detector, corresponding to the measurement θ_z .

2. **Create a projection on the (x, y) pixel plane of the maximum values along the z axis.**

A single measurement can not be used to define the ROI as the different diffraction spots will appear or disappear for different values of z , so it is convenient to work on a 2D projection on the (x, y) plane of all the maximum values of each pixel along the z axis, i.e. each element (x, y) of the projection will contain the maximum value of the corresponding pixel among all measurements of the specific session. In this way any relevant increase of neutron counts for each pixel in the whole measurement session will be taken into account.

3. **Find the coordinates (x, y, z) of the pixel with the absolute maximum counts**

The pixel with the absolute highest neutron count is part to the central spot, so its coordinates $p_{max} = [x_{max}, y_{max}]$ can be used to approximately identify the position of the 0th order on the 2D detector.

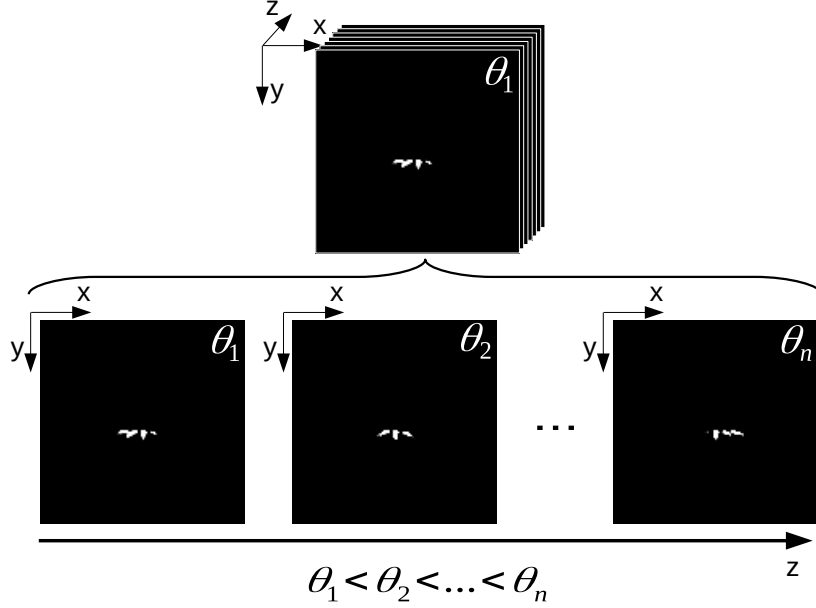


Figure 4.7: 3D array containing all the measurements θ_z for a measurement session of fixed tilt angle ζ .

4. **Define an approximate range for the limiting rows of the ROI and use the signal-to-noise ratio (S/N) to find the first row**

As shown in figure 4.3 and explained in subsection 4.1.1 the longest diffraction spots in the y direction among the different tilt angles are the ones for $\zeta = 0$ deg, with an approximate length of 11 pixels. It can be therefore assumed that the limiting rows of the ROI will always be somewhere in the range $[y_{max} - 12, y_{max} + 12]$. It is expected that in the pixels where the diffraction spots are present the neutron counts will significantly increase compared to the background noise, so checking for significant variations in the S/N can be used to find the first row y_1 . The algorithm uses the aforementioned 2D projection to check for increments of $S/N > 2$ along the column x_{max} starting from the top $y = 0$. To discard isolated fluctuations, the increment has to be valid for three consecutive pixels.

Algorithm A.1 in appendix A.2 shows the Python code used to find the first row y_1 of the ROI. The same procedure can be repeated starting from the bottom ($y = 127$) to define the lowest row y_2 of the ROI. In a similar way it is possible to find the limiting columns for each row of the region $[y_1, y_2]$ starting from the left and from the right ($x = 0$ and $x = 127$). The only difference between the procedure used to define the rows and the one used to define

the columns is that due to the shape of the spots a less strict condition has been applied to the increment in S/N. When defining the columns the spots might only extend for 2 consecutive pixels and the increment in S/N ratio is smoother compared to the rows so the algorithm checks for 2 consecutive pixels with $S/N > 1.5$ for the first pixel and $S/N > 2$ for the second.

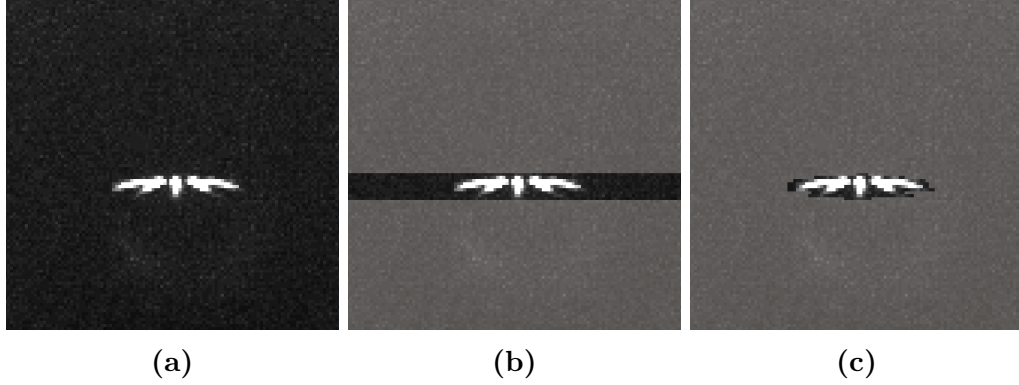


Figure 4.8: Visual representation of the effect of the ROI search algorithm: (a) 2D projection on the (x, y) pixel plane of the maximum values along z , (b) Limiting rows of the ROI, and (c) final result. The discarded pixels are highlighted with a brighter shade.

An example of the results from this procedure is shown in figure 4.8. The same figure has been created for each measurement session to ensure that the algorithm produced valid outcomes.

4.2.2 Estimation of the incident angle of the measurements

In the case of a perfectly sinusoidal grating and a perfectly monochromatic non-divergent beam, the diffraction efficiency of the 0th order is symmetric in respect to $\theta = 0$. These can be seen from the invariance of equation 2.25 under the transformation $\theta \rightarrow -\theta$ for $j = 0$. As a consequence, the intensity of the 0th order spot should reach its minimum for the symmetric values θ_{min} and $-\theta_{min}$.

This is not expected in the case of an imperfect grating and an imperfect beam. The minima of the intensity of the 0th order can still be used for an estimation of the measurement z_0 (z being the number of the measurement as indicated in the previous section) defined as corresponding to the hypothetical measurement of incident angle $\theta_{z_0} = 0$. The term "hypothetical" has been used because θ_{z_0} does not necessarily belong to the set of data collected

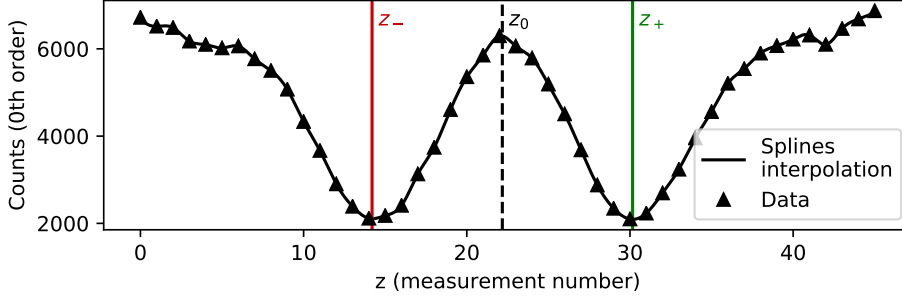


Figure 4.9: Example of estimation of z_0 with $\theta_{z_0} = 0$ (using the 0th order of $\zeta = 40$ deg).

in each session, as for the values θ_{z_-} and θ_{z_+} corresponding to the minima of the intensity before and after θ_{z_0} , respectively.

In order to overcome the limited sampling frequency of the measurements, the data points have been interpolated using cubic splines and the value of $z_0 = (z_- + z_+)/2$ has been found as shown in figure 4.9. Some of the measurement sessions stop before the intensity of the 0th order reaches the second minimum as shown in figure 4.10. In these cases the position of $\theta = 0$ is arbitrarily defined in each case using the first minimum and the profile shape as an indication.

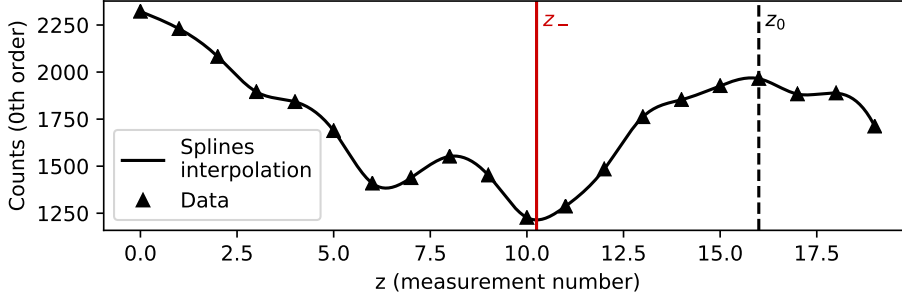


Figure 4.10: Example of estimation of z_0 with only one minimum ($\zeta = 80$ deg).

Once the value z_0 has been defined, the incident angle associated with each measurement z can be found as

$$\theta_z = (z - z_0) \cdot \delta\theta \quad (4.1)$$

where $\delta\theta$ is the step-width of the measurement session. In order to take into account any deviation from the estimated value of z_0 , an off-set value θ_0 is given as a free parameter during the fitting of the data.

4.2.3 Neutron counts

Let us indicate the number of counts of a specific diffraction order $j = 0, \pm 1, \pm 2, \dots$ as N_j and its relative diffraction efficiency as η_j . The latter quantity can be expressed as:

$$\eta_j = \frac{N_j}{\sum_{i=-m}^m N_i} \quad (4.2)$$

where $2m + 1$ is the number of diffracted waves. Once the ROI has been defined the neutron counts in each row have to be allocated to the different diffraction orders.

Despite the 0th order being easily identifiable, as explained in subsection 4.1.2, the 1st and the 2nd orders overlap for some values of θ as shown in figure 4.4. In order to calculate the diffraction efficiencies, it is necessary to distribute the counts in the overlapping region between the 1st and the 2nd order of diffraction. The intensity profile of each row has been approximated and fitted by a sum of Gaussian functions

$$P(x) = \sum_{j=-m}^m A_j \exp^{(x-\bar{x}_j)^2/\sigma_j^2} = \sum_{j=-m}^m G_j(x) \quad (4.3)$$

as shown in figure 4.11.

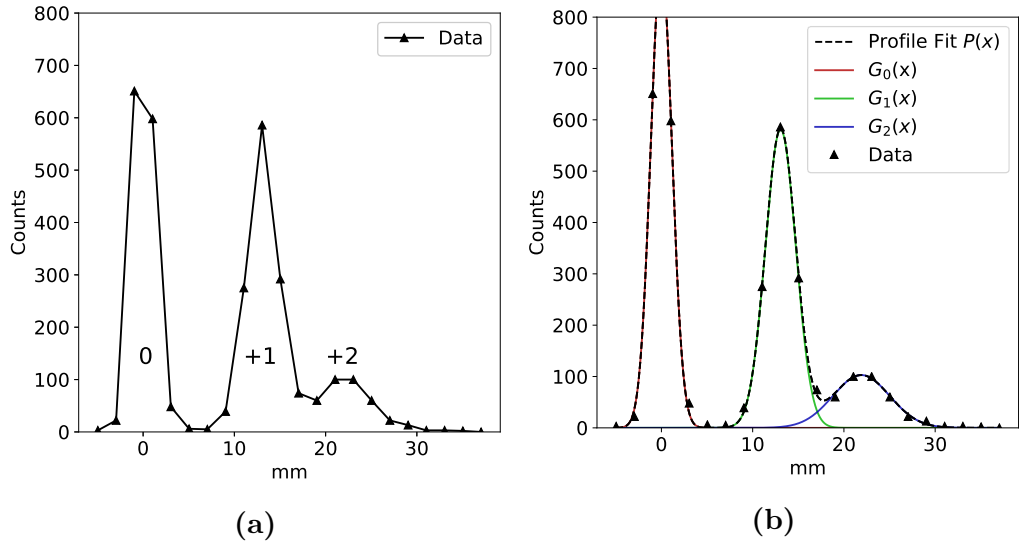


Figure 4.11: (a) Row intensity profile. (b) Fit with sum of Gaussian functions.

Let us consider the case shown in figure 4.11 and use the Gaussian distributions derived from the fit to divide the x-axis in four regions as shown in figure 4.12:

- Region 1: 0th order $\rightarrow x \in [\bar{x}_0 - 3.5\sigma_0, \bar{x}_0 + 3.5\sigma_0]$
- Region 2: 1st order, excluding the overlap with the 2nd order $\rightarrow x \in (\bar{x}_0 + 3.5\sigma_0, \bar{x}_2 - 3.5\sigma_2]$
- Region 3: Overlap region $\rightarrow x \in (\bar{x}_2 - 3.5\sigma_2, \bar{x}_1 + 3.5\sigma_1]$
- Region 4: 2nd order, excluding the overlap with the 1st order $\rightarrow x \in (\bar{x}_1 + 3.5\sigma_1, \text{end of ROI}]$.

In regions 1, 2 and 4 the raw data is distributed among the relative diffraction order without any correction. In region 3 the raw data are distributed between the 1st and the 2nd order according to the ratio of the corresponding Gaussian functions derived from the fit. For example: for the point x_a belonging to the overlap region with corresponding raw data value y_a , the value will be distributed as

$$\begin{aligned} y_a \frac{G_1(x_a)}{G_1(x_a) + G_2(x_a)} &\rightarrow \text{1st order} \\ y_a \frac{G_2(x_a)}{G_1(x_a) + G_2(x_a)} &\rightarrow \text{2nd order} \end{aligned} \quad (4.4)$$

Once the neutron counts are assigned to the relative diffraction orders, the diffraction efficiencies are calculated using equation 4.2.

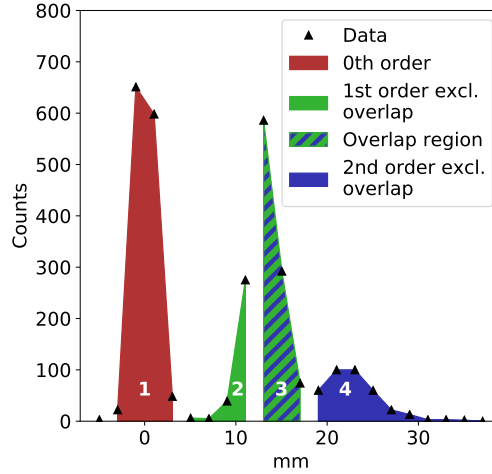


Figure 4.12: Location of diffracted peaks and overlapping region defined using the fit of sum of Gaussian distributions from equation 4.3.

4.2.4 Uncertainties

In a neutron experiment as the one discussed in this thesis, each measurement takes a considerable amount of time: between 30 min and 1.5 hours to obtain a relevant number of counts. Therefore, trying to define the uncertainties for each session by taking multiple measurements of the same position for a statistically relevant number of times would be very impractical, and in absence of such measurements a different method is needed.

In the pixel area far from the ROI, the neutron counts do not go to zero despite the collimation, and some useful information about the uncertainties might be extracted from there. Measurements with the neutron beam shutter closed have been performed to investigate external sources of noise and the results showed a neglectable background. As assumed, these counts outside the ROI are simply due to neutrons randomly scattered by the aperture edges, the tubes, the sample holder and the sample itself.

By plotting a histogram of a randomly selected pixel region outside the ROI all measurements present a Poisson distribution of the counts as shown in figure 4.13. It can be observed that the average of the distribution increases with the measurement time as expected for a Poisson process. Therefore, we may assume that a similar behaviour would be observed for a group of pixels from within the ROI and that the neutron counts will follow the same statistics for each single measurement. Consequently, taking an uncertainty of $\Delta N_j = \sqrt{N_j}$ is, indeed, an appropriate choice.

By taking the formula for the diffraction efficiencies shown in equation 4.2,

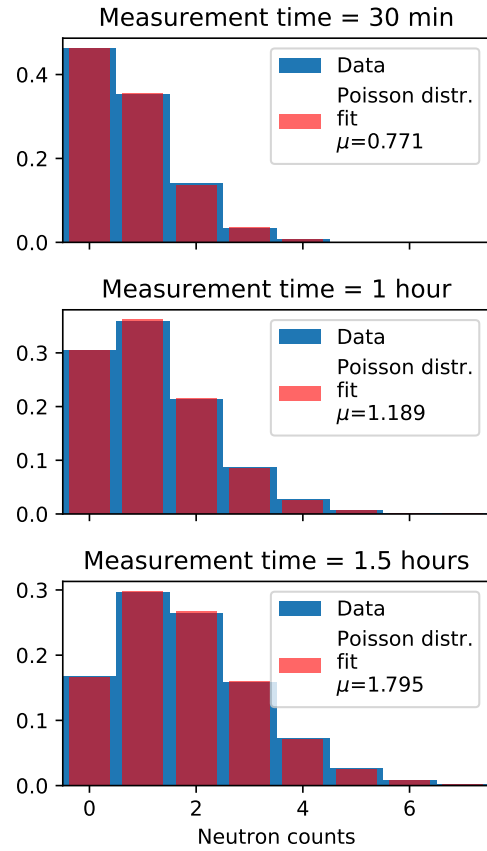


Figure 4.13: Neutron counts outside of the ROI for sessions with different exposure times fitted with a Poisson distribution $P(k) = e^{-\mu} \frac{\mu^k}{k!}$.

we can calculate the error propagation as

$$\begin{aligned}
 \eta_j &= \frac{N_j}{\sum_{i=-m}^m N_i} \Rightarrow \Delta\eta_j = \sum_{i=-m}^m \frac{\partial\eta_j}{\partial N_i} \Delta N_i = \\
 &= \sum_{i=-m}^m \left(\frac{N_j}{(\sum_{l=-m}^m N_l)^2} + \frac{1}{\sum_{l=-m}^m N_l} \right) \Delta N_i = \\
 &= \frac{\eta_j^2 + \eta_j}{N_j} \sum_{i=-m}^m \Delta N_i = \frac{\eta_j^2 + \eta_j}{N_j} \sum_{i=-m}^m \sqrt{N_i}
 \end{aligned} \tag{4.5}$$

4.3 Observation of the Pendellösung interference

One important result that is possible to obtain after the computation of the diffraction efficiencies is the observation of the Pendellösung interference. In subsection 2.1.3 it is shown that the Pendellösung interference results in a modulation of the diffracted waves amplitudes for different thicknesses. This will, as a consequence, also determine the maximum value achievable by the diffraction efficiencies of the 1st and 2nd order for distinct tilt angles. The latter are shown in figure 4.14 for the orders -1 and -2: the data clearly indicate a modulation of the amplitudes of the diffracted waves for different values of the tilt angle ζ , which determines the effective thickness.

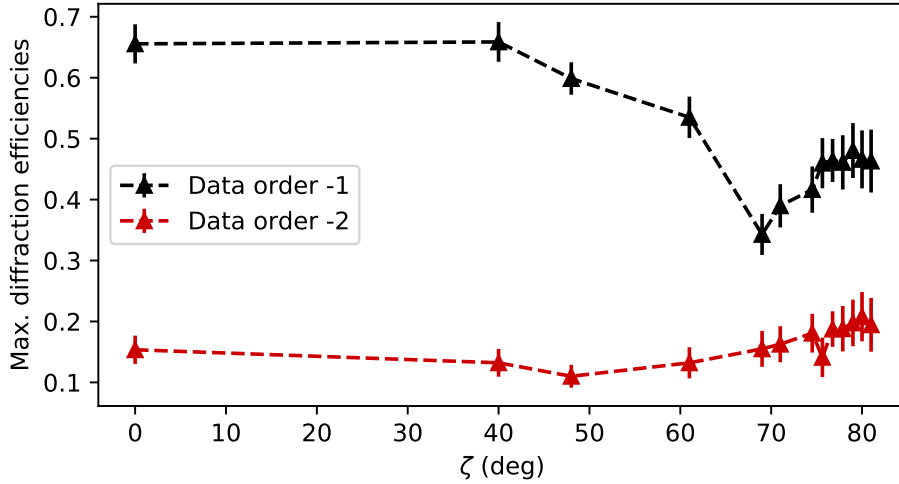


Figure 4.14: *Experimental observation of Pendellösung interference extracted from the analysed data set*

4.4 Wavelength distribution and beam divergence

Up to this point the theory assumes a monochromatic and perfectly collimated beam. In order to be used to fit the experimental data it needs to be extended to the more realistic case of having a wavelength distribution of neutrons in a divergent beam.

4.4.1 Wavelength distribution

Let us consider a monochromatic (M) and perfectly parallel (P) beam diffracted by a grating resulting in $\eta_{MP}(\lambda, \theta)$, where λ is the wavelength of the incoming neutrons and θ is the angle of incidence. In presence of a wavelength distribution $\rho(\lambda)$ for a fixed value of θ the contribution of the different wavelengths will result in the following:

$$\eta_P(\theta, \lambda) = \int \rho(\lambda) \eta_{MP}(\lambda, \theta) d\lambda \quad (4.6)$$

Despite the monochromatic case requiring to solve numerically a fairly simple differential equation, extending that procedure to take into account a wavelength distribution might considerably increase the computational time.

The process could be made more efficient by using a weighted sampling of the distribution reducing the number of points necessary for an accurate result of the integral. Instead of choosing equally spaced points on the wavelengths axis the points get distributed with different densities following the probability profile; figure 4.15 shows an example for a simple Gaussian distribution. One way to achieve this is to exploit inverse transform sampling, which is generally used for generating sample numbers at random from any probability distribution function given its cumulative distribution function (CDF) [28]. A visualisation of this procedure is shown in figure 4.16: a uni-

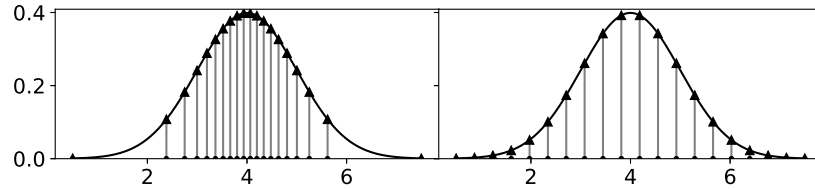


Figure 4.15: *Example of weighted sampling for a general Gaussian distribution (left) compared to uniform sampling (right) produced by the same number of points.*

form interval of values on the y axis of the CDF corresponds to a series of points on the x axis with sampling density distributed according to the PDF.

As explained in section 3.3, a measurement of the wavelength distribution around the point of highest intensity of the beam showed an exponentially modified Gaussian (EMG) shape with $\lambda_{max} \approx 3.7 \text{ nm}$ which, however, is not representative for different sections of the neutron beam. During the course of the experiment, as mentioned in subsection 4.1.1, the position of the diffracted spots on the detector moved between measurement sessions indicating a change in the experimental set-up and probably the selection of a different part of the neutron beam. In addition, tilting the sample causes the cadmium frame to cut off part of the incoming neutron beam as shown in figure 4.3, and this could further affect the wavelength distribution. As a starting point for the fitting of the data, the function chosen as profile of the wavelength distribution was the one shown figure 3.8 but, as expected, the fit did not yield reasonable results due to the aforementioned reasons. The distribution profile used in the fits is still assumed to have an EMG shape and the parameters μ , σ and τ are given as free variables.

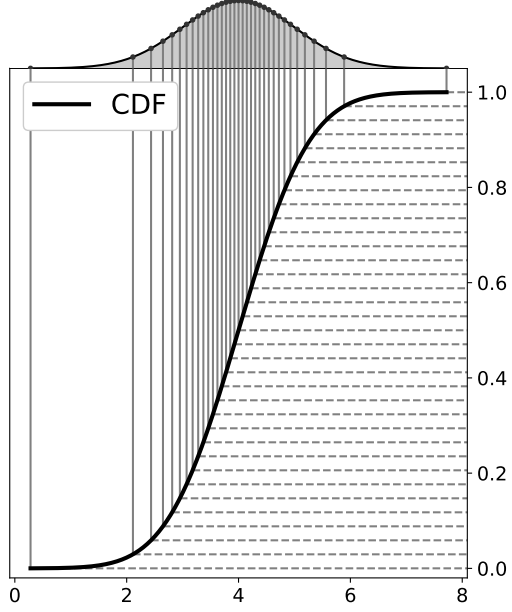


Figure 4.16: *Example of inverse transform sampling.*

4.4.2 Beam divergence

When the diffraction efficiencies are calculated numerically, for each wavelength λ_i the solution is computed directly of all incident angles θ ; this is an arbitrary choice as doing the opposite would also be a valid option. Once the correction for the wavelength distribution is applied and the diffraction efficiencies are calculated for a perfectly parallel beam, the effect of a divergence with profile $B(\theta)$ can be computed as

$$\eta(\theta, \lambda) = \int \eta_P(\lambda, \tilde{\theta}) B(\theta - \tilde{\theta}) d\tilde{\theta} = [\eta_P * B](\theta) \quad (4.7)$$

which is a convolution of the diffraction efficiency of a perfectly parallel beam with the beam profile.

As in the case of the wavelength distribution, calculating the diffraction efficiencies for a high number of angles θ would significantly increase the computational time. So, to make the process more efficient, only a limited number of intermediate points are calculated and the rest is obtained through cubic splines interpolation. For some tilt angles ζ the diffraction efficiencies oscillate quickly between different incident angles. To make sure the splines are an appropriate approximation also in such cases, the number of intermediate points has been assigned ensuring a discrepancy of maximum 10^{-4} .

As explained in subsection 4.1.1, a Gaussian curve seems to describe properly the horizontal profile of the neutron beam. Accordingly, the following beam profile has been chosen for the fit:

$$B(\theta) = \frac{1}{\sqrt{2\pi}\sigma_{div}} e^{(\theta-\tilde{\theta})^2/(2\sigma_{div})^2} \quad (4.8)$$

with the divergence parameter $\sigma_{div} = 0.00035$ rad.

4.5 Fits results

In the following, the results obtained from the fitting of the data are presented. The models assumes an average index of diffraction $n_0 = 1$ inside the grating and 5 diffraction orders, i.e. 9 coupled waves: 0, ± 1 , ± 2 , ± 3 , ± 4 . The python module of Statistical functions (scipy.stats) [29] offers a variety of tools to deal with probability distributions including the EMG [30]. In the software the parameters defining the shape of the EMG are μ , σ and $K = \tau/\sigma$, the same will be used here.

Glossary of fit parameters	
Parameters	Description
$b_c \Delta \rho_i$	Modulation strength of the i-th Fourier component
ϕ_i	Phase of the i-th Fourier component
μ , σ and K	EMG wavelength distribution variables
σ_{div}	Divergence parameter (Gaussian profile)
θ_0	Incident angle off-set

Table 4.2: *Glossary of fit parameters*

4.5.1 Perfectly sinusoidal grating with fixed wavelength distribution

Free parameters: $b_c \Delta \rho_1, \theta_0$ (See table 4.2)

Diffraction efficiencies

The first fit session has been carried out assuming a perfectly sinusoidal profile of the grating

$$n(\vec{r}) = n_0 + \Delta n_1 \cos(\vec{G} \cdot \vec{r}) = n_0 + \Delta n_1 \cos\left(\frac{2\pi}{\Lambda} x\right) \quad (4.9)$$

and, as anticipated, the initial choice for the profile of the wavelength distribution was the one shown in figure 3.8 with

$$\begin{cases} \mu \approx 3.37 \text{ nm} \\ \sigma \approx 0.19 \text{ nm} \\ \tau \approx 0.80 \text{ nm} \end{cases} \quad (4.10)$$

which, as expected, did not yield acceptable results.

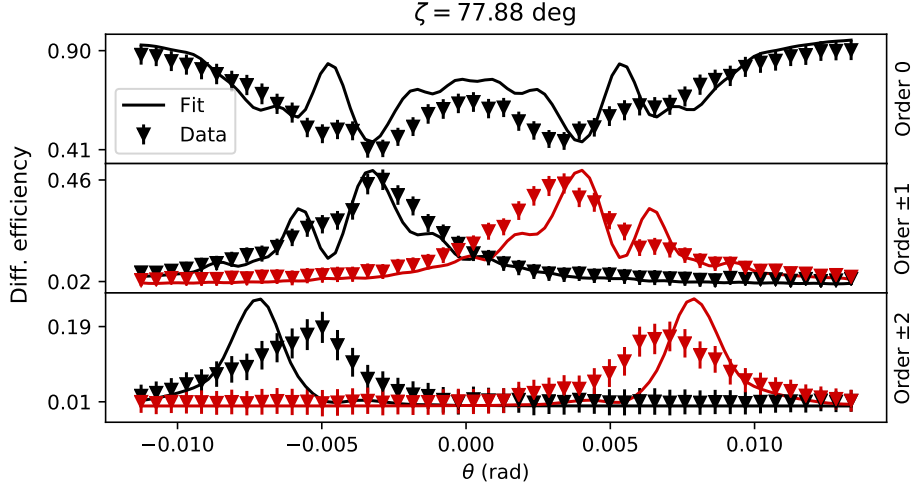


Figure 4.17: *Fit results for and $\zeta = 77.88$.*

The diffraction efficiencies oscillate too prominently compared to the data. This discrepancy is more noticeable for high tilt angles where the oscillations

are accentuated by the increased thickness, as shown in figure 4.17. Moreover, the peaks and the minima of the curves appear shifted and in general the data seems to have a more gentle slope. These effects can be attributed both to the shape of the wavelength distribution and to an underestimation of the beam divergence.

Despite the latter, the data do not show any relevant difference in the width of the central spot among different tilt angles. To exclude an error in the divergence estimation a new fit has been executed with σ_{div} as an additional free parameter. The outcomes seem to slightly improve for low tilt angles, while for high tilt angles the oscillations are too washed out to match the data, as shown in figure 4.18; other effects may play a more prominent role. Moreover, for both low and high tilt angles the position of the peaks and minima are still shifted and the value of the divergence parameters raises above 0.001 rad, implying a beam half-divergence $\Delta\theta > 0.002$ which is unreasonable. These results indicate that the divergence might not be the cause of the low accuracy of the fit so μ , σ and K are given as free parameters.

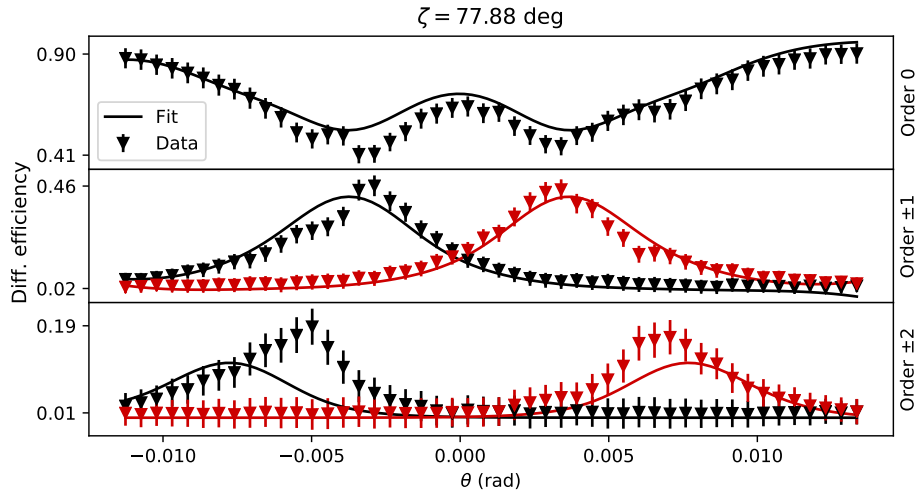


Figure 4.18: *Fit results for $\zeta = 77.88$ with σ_{div} as additional free parameter.*

Pendellösung interference

Figure 4.19 shows the data from figure 4.14 together with the values predicted by the model. As expected, also in this regard there is a significant discrepancy between the fit results and the experimental data.

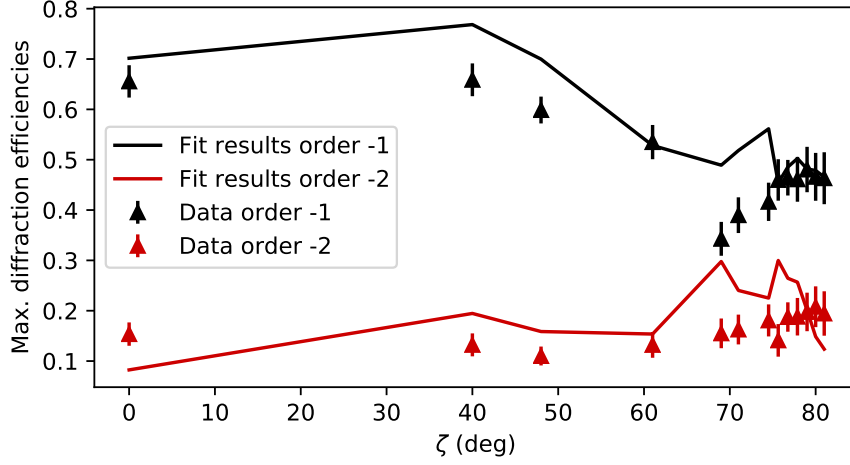


Figure 4.19: Plot of the maximum diffraction efficiencies predicted for the orders -1 and -2 compared with experimental data, according to the model of subsection 4.5.1

4.5.2 Perfectly sinusoidal grating with free parameters for the wavelength distribution

Free parameters: $b_c \Delta \rho_1, \theta_0, \mu, \sigma, K$ (See table 4.2)

Diffraction efficiencies

Allowing the EMG shape of the wavelength distribution to vary improves the results for both low and high tilt angles, in terms of oscillations of the diffraction efficiencies and matching of the maxima and minima. Interestingly, all the fitted curves are able to match the peaks of the 1st order of diffraction while 9 out of 13 can not reach the measured value of the 2nd order of diffraction; two examples are shown in figure 4.20.

The wavelength distributions resulting from the fits of the data seem to be consistent with the groups presented in table 4.1. The measurement at $\zeta = 40$ deg, which was executed before the first change of set-up mentioned in subsection 4.1.1, shows a wavelength distribution different from the other two groups as shown in figure 4.21. The EMG shape at $\zeta = 40$ deg presents value of $\lambda_{max} = 3.9$ which is not too far from what is expected based on the measurement shown in figure 3.8, however the relative width $\Delta\lambda/\lambda_{mean} \approx 0.6$ is twice as large.

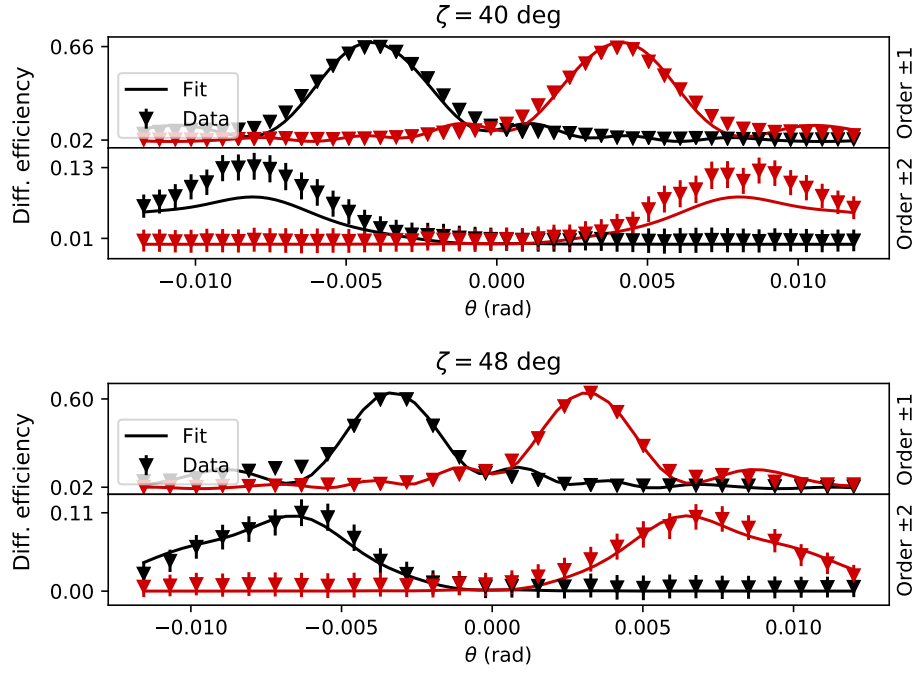


Figure 4.20: Fit results for 1st and 2nd diffraction order with $\zeta = 40$ deg (top) and $\zeta = 48$ (bottom).

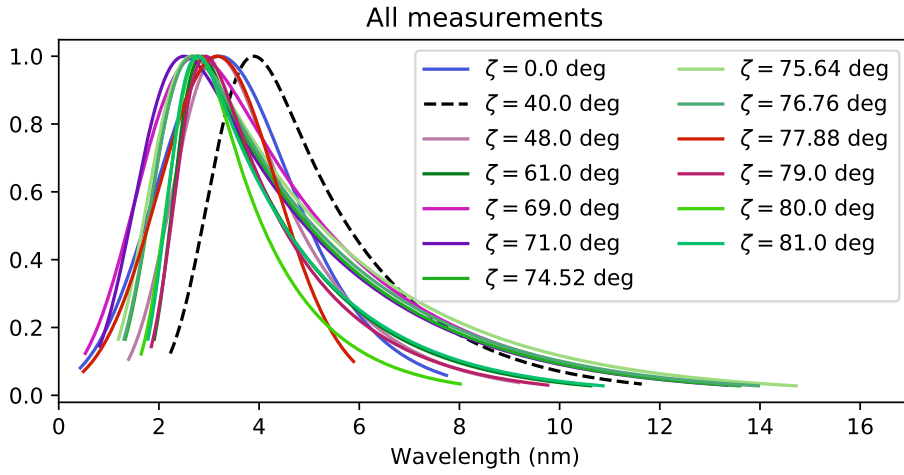


Figure 4.21: Wavelength distributions according to fit results for all measurements

The wavelength distributions of groups 2 and 3 exhibit in general shorter mean and maximum wavelengths. In particular, group 3 presents a sys-

tematic decreasing of the maximum wavelength for increasing tilt angles, as shown in figure 4.22 (top). This could be interpreted as the cadmium frame cutting off the bottom part of the beam and, consequently, the longer wavelengths. However, the same behaviour is not observed for group 2. Overall, the results seem to highlight a significant difference in terms of wavelength in group 1.

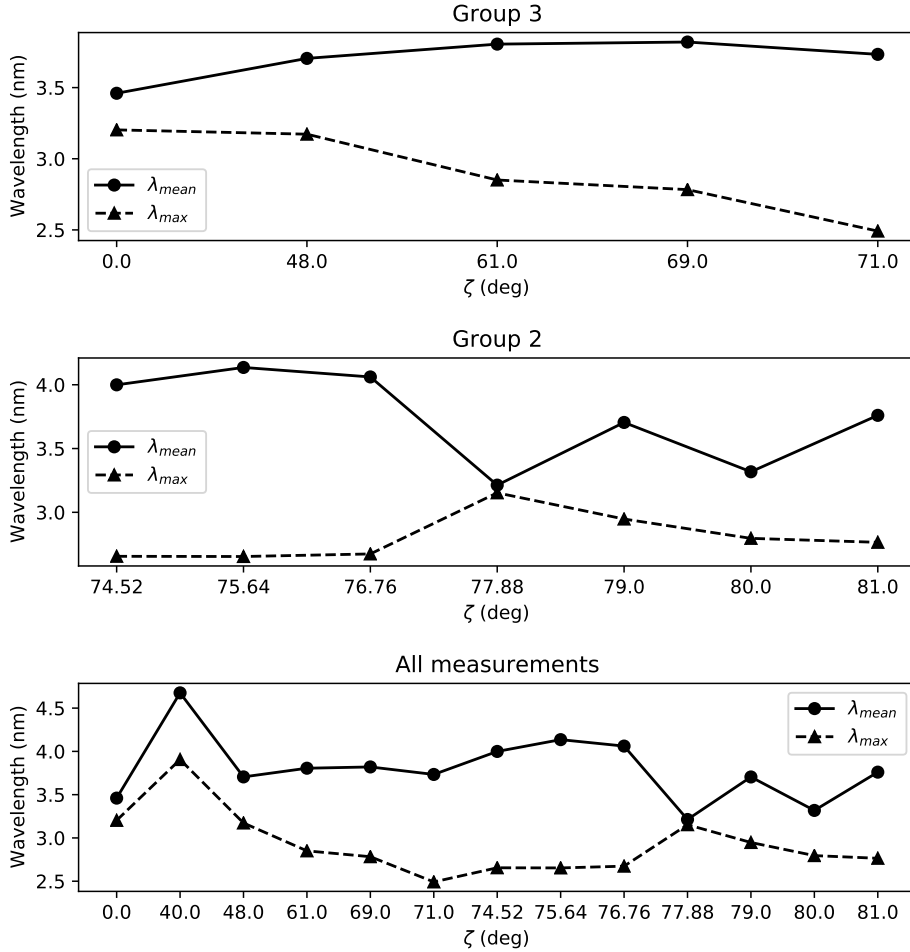


Figure 4.22: Evolution of $\lambda_{mean}/\lambda_{max}$ for different tilt angles according to fit results for group 3 (top), group 2 (center) and all measurements (bottom)

The scattering length-density modulation parameter presents an average value of $b_c \Delta \rho_{1,avg} \approx 10.7 \pm 0.2 \text{ 1}/\mu\text{m}^2$ and a tendency to increase for high tilt angles, as shown in figure 4.23. The reason for this is unclear. One would expect that an increase in the thickness would lead to an increase of incoherent scattering, therefore reducing the modulation strength and a

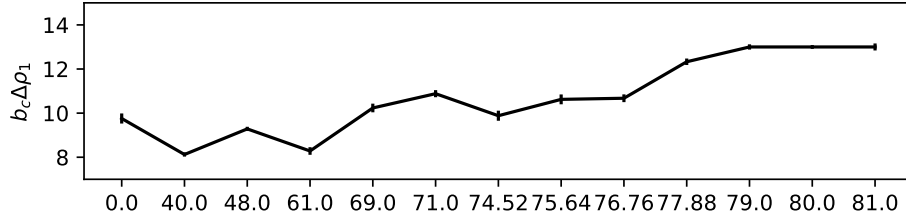


Figure 4.23: *Fit results for the scattering length-density modulation parameter $b_c \Delta \rho_1$*

decrease in the effect. The results indicate the opposite tendency. One possibility is that the EMG shape is not able to follow the changes in the wavelength distribution and this affects the other parameters, but the latter can not be inferred simply based on this idea.

The model used up to this point does not predict any asymmetry in the diffraction efficiencies in respect to $\theta = 0$, but the data for high tilt angles seem to present one. This can be seen in figure 4.24 where it is more noticeable for the 2nd order of diffraction. Initially, it was suspected that the asymmetry was just a product of some mistake in the calculation of the diffracted waves intensities, so the procedure has been retraced step by step, but no error was found. Plotting the intensity of the 0th order spot without any manipulation already shows an asymmetric behaviour for $\zeta = 76.76$, 77.88 and 75.64 deg, the latter shown in figure 4.25, and this might be an indication that it is not deriving from a computational mistake.

The deviation from the symmetric shape can be caused by multiple factors, such as: a flaw in the experimental set-up, strong imperfections in the diffraction grating, unexpected non-linearity in the step-width along θ due to the tilt of the sample, or phase effects from higher component of the gratings. Without the possibility of running some tests, or at least extend the measurements to a range of θ sufficiently large to observe both sides of the diffraction orders for all sessions, it is difficult to infer which of the aforementioned causes might be relevant. However, it is believed that a strong imperfection of the grating structure might affect in similar ways the curves of both low and high tilt angles, while the available data suggest a dependence on the tilt angle. In the laboratory log book there is no evidence of any set-up characteristic that might induce this effect, but this option can not be ruled out.

Inferring a possible non-linearity in the step-width is unfeasible with the information available. Since the majority of the fitted curves are unable to reach the peaks of the second diffraction order, a second Fourier component

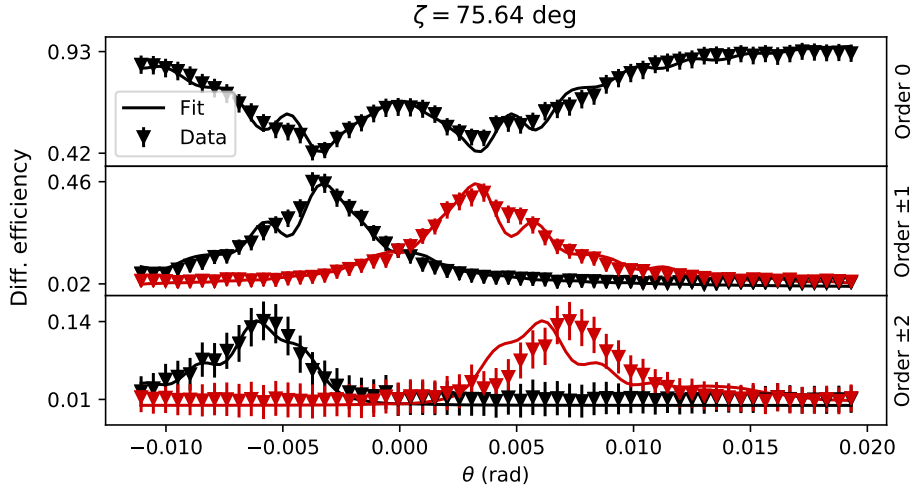


Figure 4.24: Fit results for $\zeta = 75.64$ deg showing accentuated asymmetry for the 2nd diffraction order.

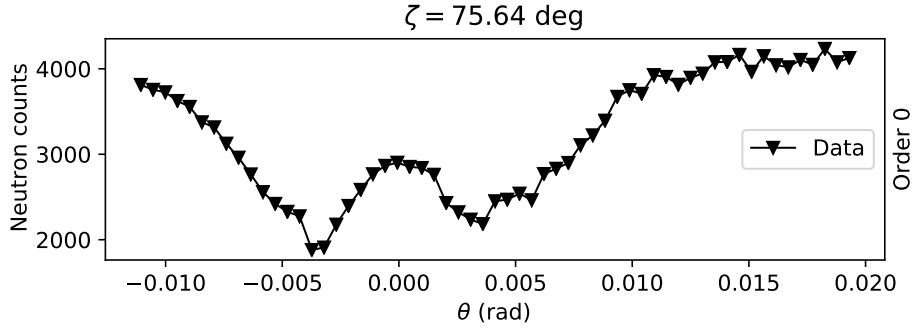


Figure 4.25: Intensity of 0th diffraction order spot for $\zeta = 75.64$ deg.

of the modulation of the index of refraction has been added to the model.

Pendellösung interference

The improvements in comparison with the previous model are distinctly observable in figure 4.26. At the same time, it is possible to notice the underestimation of the second order peaks.

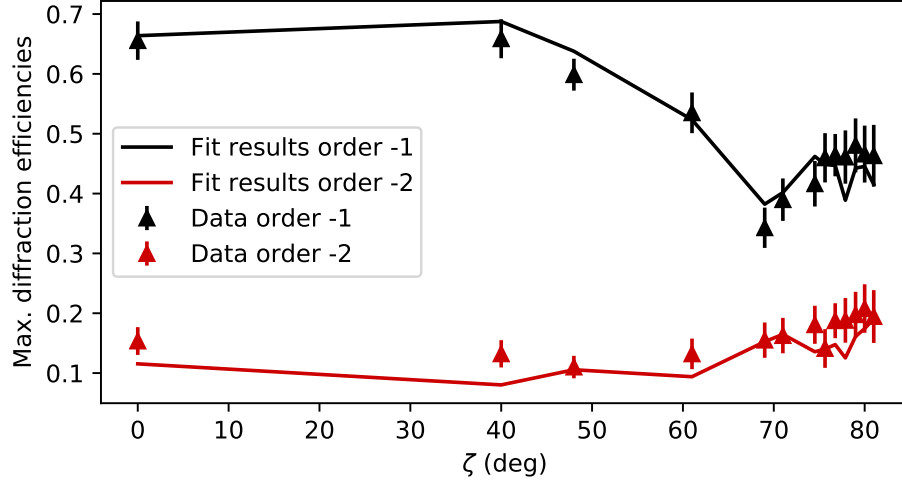


Figure 4.26: Plot of the maximum diffraction efficiencies predicted for the orders -1 and -2 compared with experimental data, according to the model presented in subsection 4.5.2

4.5.3 Diffraction grating with two Fourier components in the modulation of the refractive index

Free parameters: $b_c \Delta \rho_1, \theta_0, \mu, \sigma, K, b_c \Delta \rho_2, \phi_2$ See table 4.2

Diffraction efficiencies

With the addition of a second Fourier component in the grating profile, the refractive index will take the following form:

$$n(\vec{r}) = n_0 + \Delta n_1 \cos(\vec{G} \cdot \vec{r}) + \Delta n_2 \cos(2\vec{G} \cdot \vec{r} + \phi_2) \quad (4.11)$$

All the fitted curves together with the resulting parameters from this section are presented in appendix A.3, the square root of the diagonal terms belonging to the co-variances matrix are taken as uncertainties on fit results. The results improved for some of the measurements for which the previous model was underestimating the peaks of the second order of diffraction, as shown in figure 4.27. There were some improvements also in regard to the asymmetric shape of the second orders for some of the high tilt angles measurements. An interesting case is the one of $\zeta = 77.88$ deg shown in figure 4.28, where the asymmetric shape is almost reproduced except for some features around $\theta = -0.010$ rad and $\theta = 0.004$ rad; both points belong to ambiguous areas as

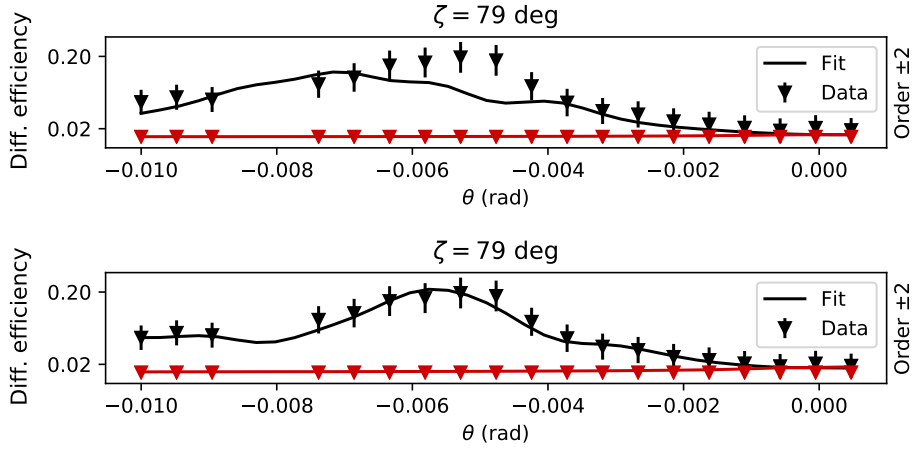


Figure 4.27: *Fit results for 1st and 2nd diffraction order with $\zeta = 79$ deg, for one (top) and two (bottom) Fourier components of the refractive index modulation.*

the former might be affected by the He pipe and the latter by the overlap of the diffracted spots, so the result might be realistic despite those particular discrepancies.

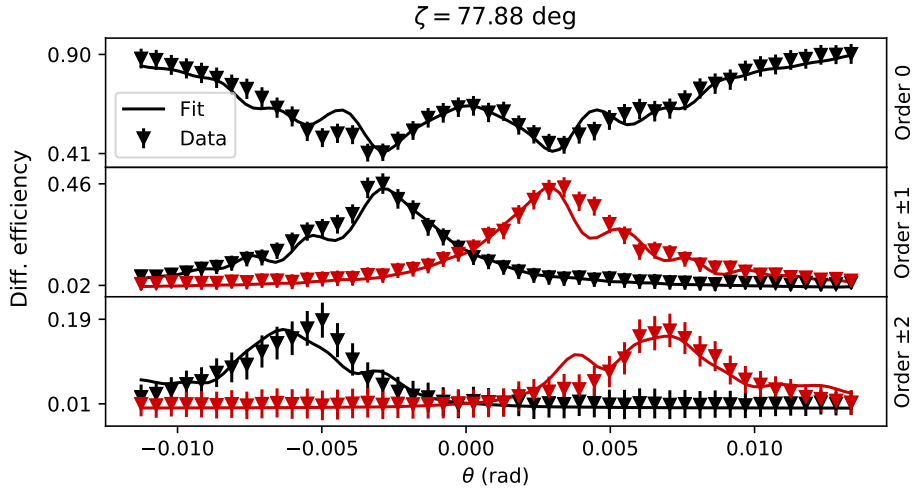


Figure 4.28: *Fit results for $\zeta = 77.88$ deg.*

The wavelength distributions derived from the results present an increased homogeneity compared to the previous case. The EMG shape of the measurement $\zeta = 40$ deg still preserves the longest mean wavelength with a value $\lambda_{mean} \approx 4.9$ nm, the mode of the distribution is reduced to a value of $\lambda_{max} \approx 3.4$ nm and the width does not vary significantly as shown

in figure 4.29.

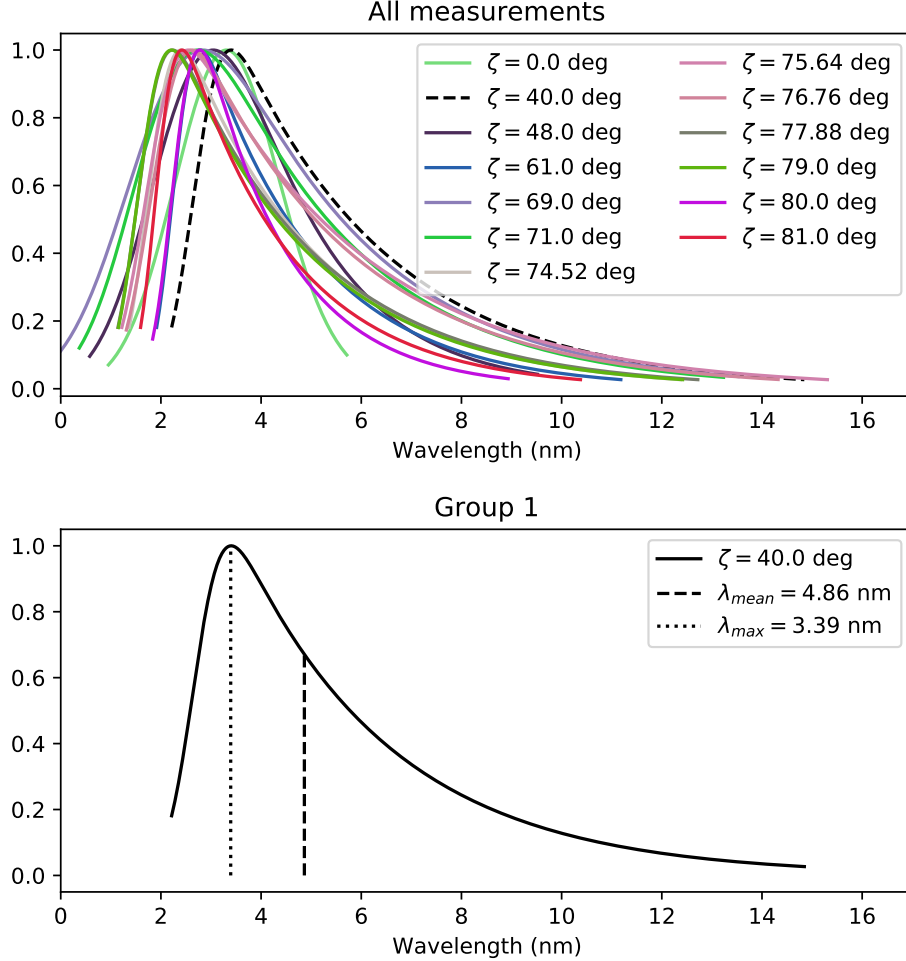


Figure 4.29: Wavelength distributions according to fit results for all measurements (top) and for $\zeta = 40$ deg (bottom).

The mean and mode wavelengths of group 3 present a different evolution for the different tilt angles, the separation between the two is more accentuated compared to the previous case. The reduction of λ_{max} for higher tilt angles is less linear. Group 2 shows a more consistent behaviour compared to the previous case, in particular for $\zeta = 77.88$ deg. The evolution of λ_{mean} and λ_{max} is shown in figure 4.30.

The scattering length-density modulation parameters $b_c \Delta \rho_1$ still present a tendency to increase for high tilt angles as shown in figure 4.23, but the slope is less prominent. The same effect is observed for $b_c \Delta \rho_2$. The average values for the modulation parameters are $b_c \Delta \rho_{1,avg} \approx 10.1 \pm 0.2$ $1/\mu m^2$ and

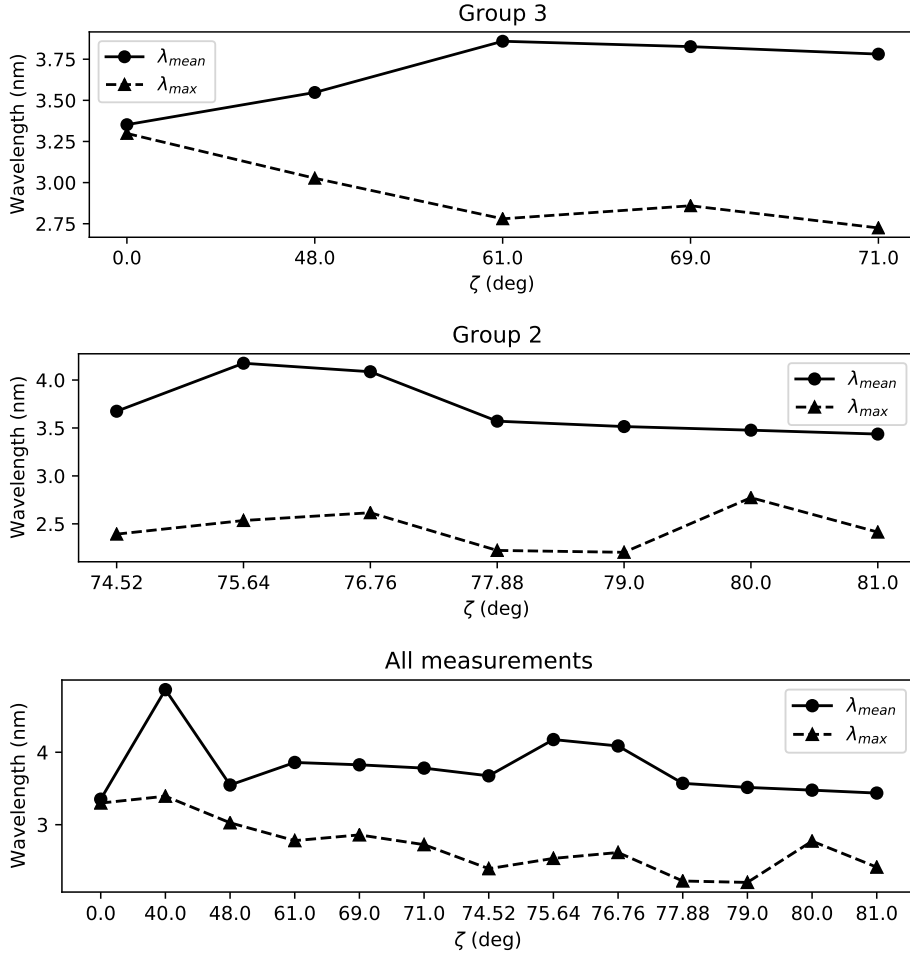


Figure 4.30: Evolution of $\lambda_{mean/max}$ for different tilt angles according to fit results for group 3 (top), group 2 (center) and all measurements (bottom)

$b_c \Delta \rho_{2,avg} \approx 3.6 \pm 0.5 \text{ } 1/\mu m^2$, the phase oscillates around an average value of $\phi_{1,avg} \approx 0.53\pi$.

Adding a second Fourier component seems to have curbed the tendency of the scattering length-density modulation parameters to increase with ζ . One might be tempted to add a third Fourier component of the refractive index modulation to additionally curb this tendency. However, in order to properly study the effects of a third component the experimental range of θ should be increased until the 3rd order of diffraction is visible. In light of these results, the data have been scanned in search of a hint for a third order of diffraction and for some measurement sessions a rather weak spot appears for large values of θ , as shown in figure 4.32. The rest of the spot is most

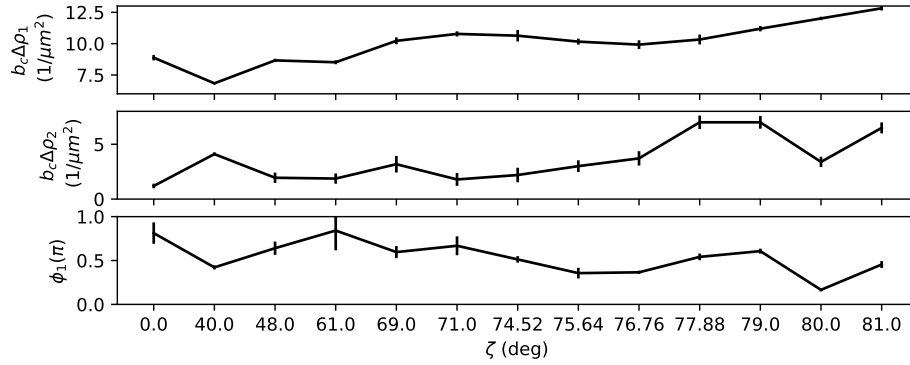


Figure 4.31: *Fit results for the scattering length-density modulation parameters and phase*

likely obscured by the helium pipes and only a few measurement sessions are performed on a θ range wide enough to observe it. Other than indicating the need of an additional Fourier component, the presence of a third order might affect the shape of the second order in the overlap region.

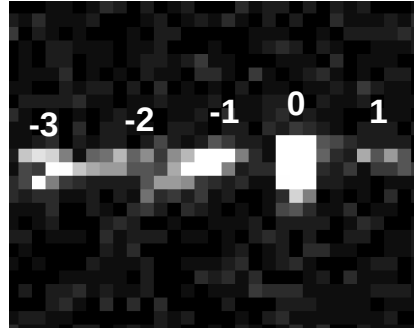


Figure 4.32: *Hint of a 3rd order of diffraction from experimental data.*

A fit session has been carried out with three Fourier components of the grating but, as expected, the results were not meaningful. The parameters presented uncertainties of more than 200% and for this reason they are not reported.

Pendellösung interference

This model is the most accurate in predicting the maximum values of the diffraction efficiencies for the orders -1 and -2 among the ones that have been tested. A plot of the diffraction efficiencies according to the model together

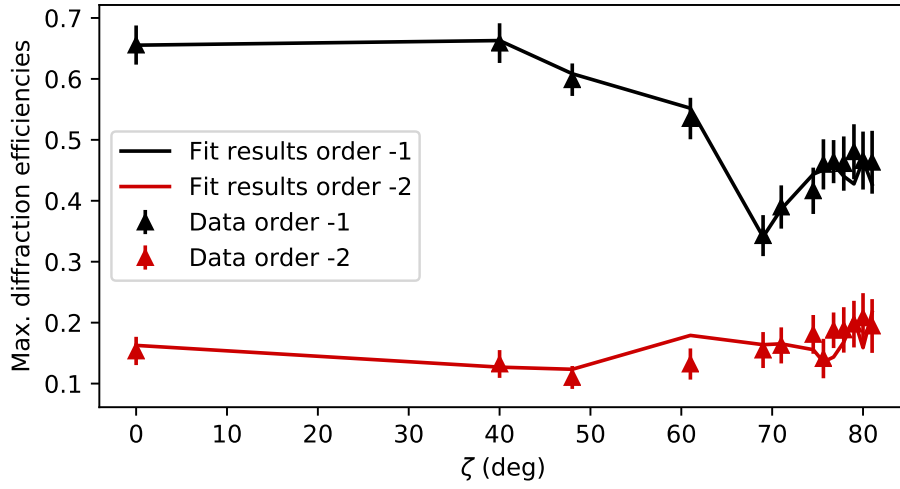


Figure 4.33: Plot of the maximum diffraction efficiencies predicted for the orders -1 and -2 compared with experimental data, according to the model presented in subsection 4.5.3.

with the data is shown in figure 4.33. In view of the above, the agreement is reasonable and provides a good description of the 1st order data behaviour.

Chapter 5

Summary and conclusions

5.1 Experimental aspects

The new analysis revealed some experimental aspects that might have affected the quality of the collected measurements. In what follows, a quick summary of such aspects is presented together with some suggestions for possible solutions to the arising issues.

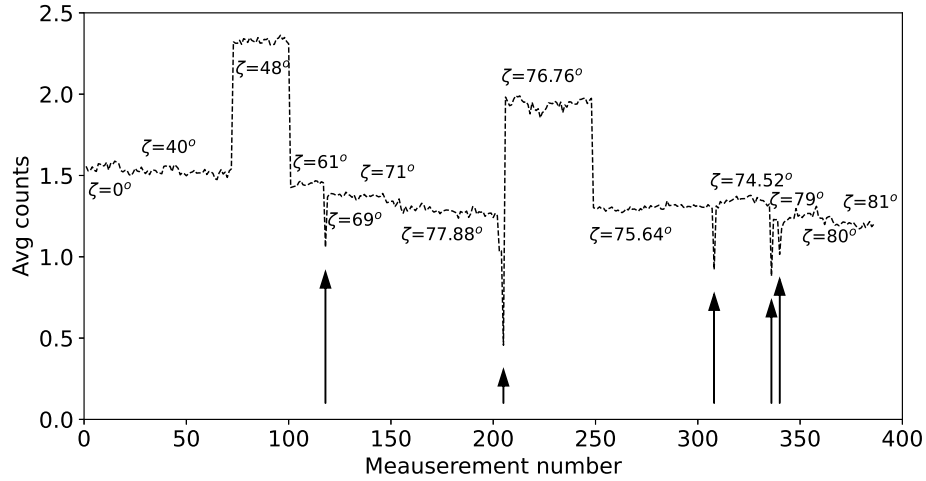


Figure 5.1: *Average total neutron counts on detector for all the collected measurement.*

Some of the data present considerable dips in neutron counts (marked by arrows in figure 5.1). These data have been discarded in the analysis. Plotting the total neutron counts at the end of each measurement (or measurement session) can disclose any relevant variation in the neutron flux,

which might be an indication of a compromised measurement that needs to be discarded or re-taken.

The spots generated on the detector by the diffracted waves are not always found in the same place: between measurement sessions the experiment setting has been modified as explained in subsection 4.1.1. Converting the measurements to images and running a quick scan of the position of the spots reveal unwanted changes in the experimental set-up.

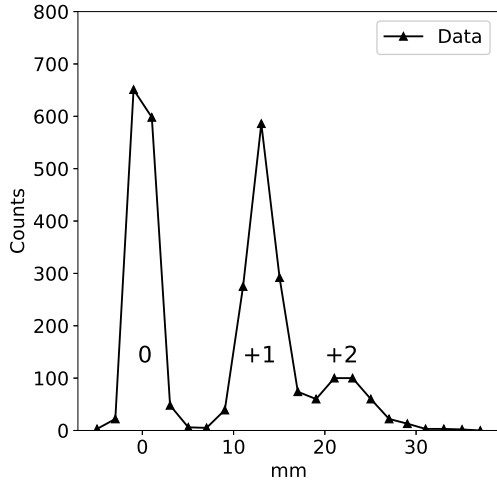


Figure 5.2: *Example of spots overlap between 1st and 2nd diffraction orders.*

brightness and contrast, as shown in figure 5.3, it is possible to see a shadow cast by the He pipes used to reduce neutron-air scattering. It is difficult to infer the position of the pipe and if it is partially shadowing the diffracted waves, but this possibility can not be rejected and it might have affected the results of the fits. Increasing the dimension of the pipes can prevent them from having any impact on the data.

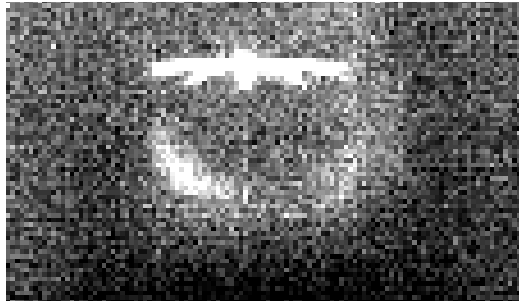


Figure 5.3: *Sum of measurements for tilt angle $\zeta = 77.88$ deg, with brightness and contrast enhanced.*

5.2 Analysis results

5.2.1 Diffraction efficiencies

A first-order multi-coupled waves theory has been used to fit the diffraction efficiencies. The model also includes a Gaussian profile for the neutron beam width and a wavelength distribution of EMG shape.

The first fit session has been carried out assuming a perfectly sinusoidal profile of the grating and a wavelength distribution of fixed shape equal to the one measured by Blaickner et al. [23] (section 3.4). As expected, the fitted curves present a severe deviation from the experimental data (figure 5.4) also because the shape of the wavelength distribution is dependent on the selected fraction of the neutron beam which varies among different measurement sessions.

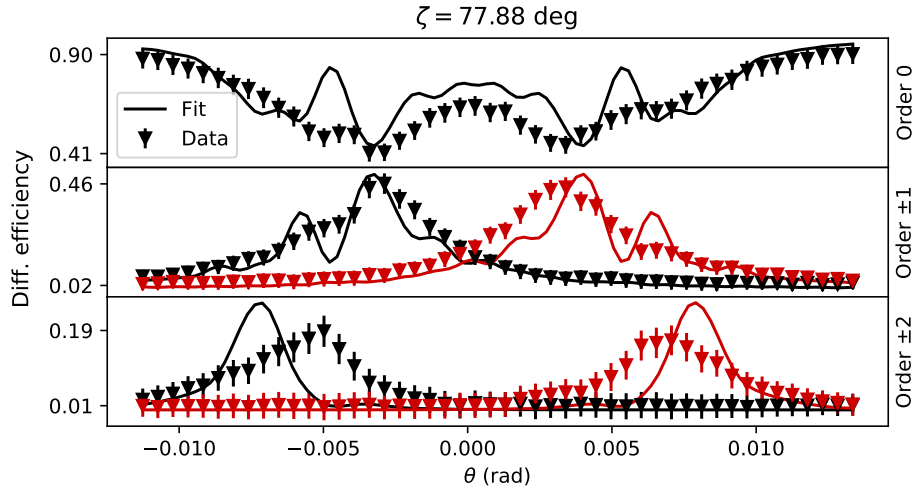


Figure 5.4: *Fit results for $\zeta = 77.88$, according to the model presented in subsec. 4.5.1*

A new fit session has then been carried out, allowing the wavelength distribution to change in shape and the results improved significantly. The wavelength distributions derived from the fit presented differences in shape that seem to be consistent with the changes in set-up mentioned in subsections 4.1.1. The fitted curves matched the peaks of the first-order diffraction efficiencies with good accuracy, but for the majority of cases they underestimated the peaks of the second orders as shown in figure 5.5. Moreover, the fitted values of the scattering length-density modulation parameter presented a tendency to increase with the higher tilt angles and the analyses also highlighted a pronounced asymmetry in θ of the diffraction efficiencies for higher

tilt angles. For the aforementioned reasons, the fit session that followed in-

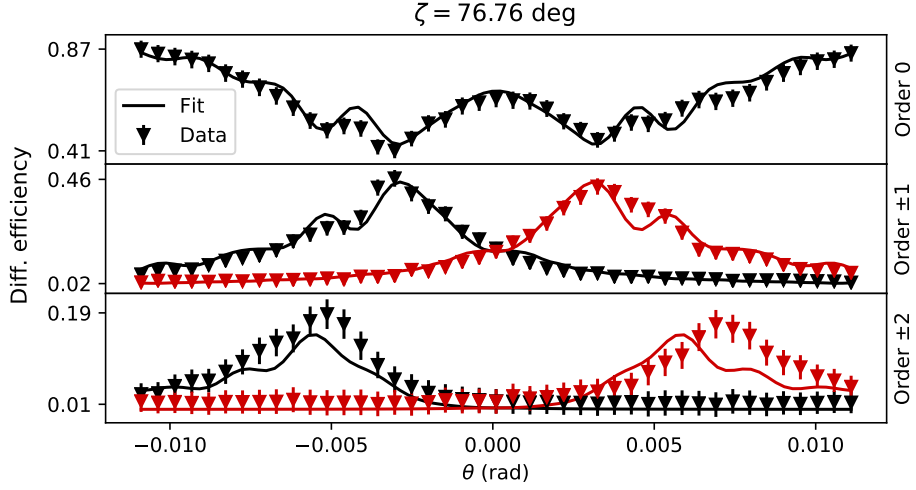


Figure 5.5: *Fit results for $\zeta = 76.76$ deg, according to the model presented in subsec. 4.5.2.*

cluded an extra Fourier component in the modulation of the refractive index. The resulting wavelength distributions presented a more homogeneous form. but still conserved the differences in shape consistent with the changes in set-up described in subsections 4.1.1.

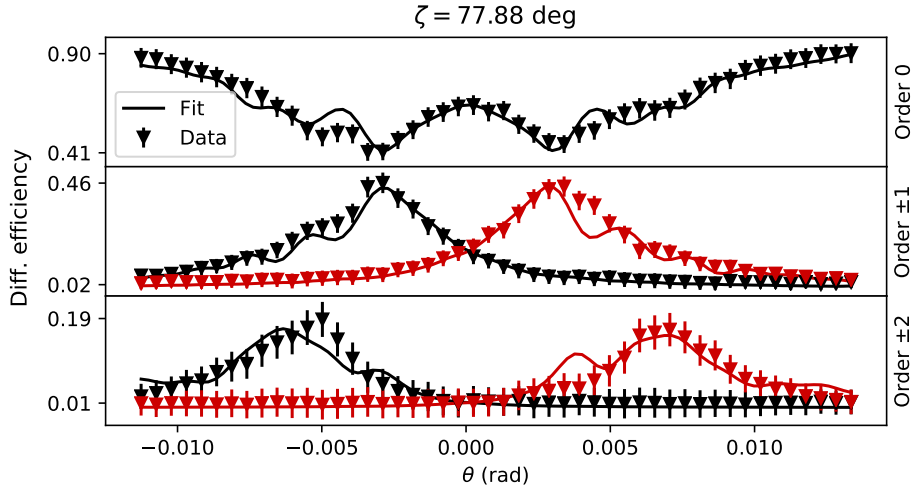


Figure 5.6: *Fit results for $\zeta = 76.76$ deg, according to the model presented in subsec. 4.5.3.*

The addition of the second Fourier component seems to attenuate the

tendency of scattering length-density modulation parameters to increase with the tilt angles. Furthermore, the majority of the curves matched the peaks of the second-order diffraction efficiencies and in some cases better match the asymmetric shape of some curves as shown in figure 5.6. Note that any discussion of χ^2_{red} values of other goodness-of-fit measures have been deliberately omitted here, since the explanatory quality of the data has not reached a level at which such discussion is meaningful.

5.2.2 Pendellösung interference

The analysis of the diffraction efficiencies for different tilt angles clearly shows a modulation of the wave amplitudes depending on the thickness of the sample. In figure 5.7, the maximum diffraction efficiencies reached by the 1st and 2nd orders of diffraction are plotted against the tilt angle. The theoretical model including a second Fourier component is able to match the peaks of the 1st and 2nd order with an acceptable accuracy.

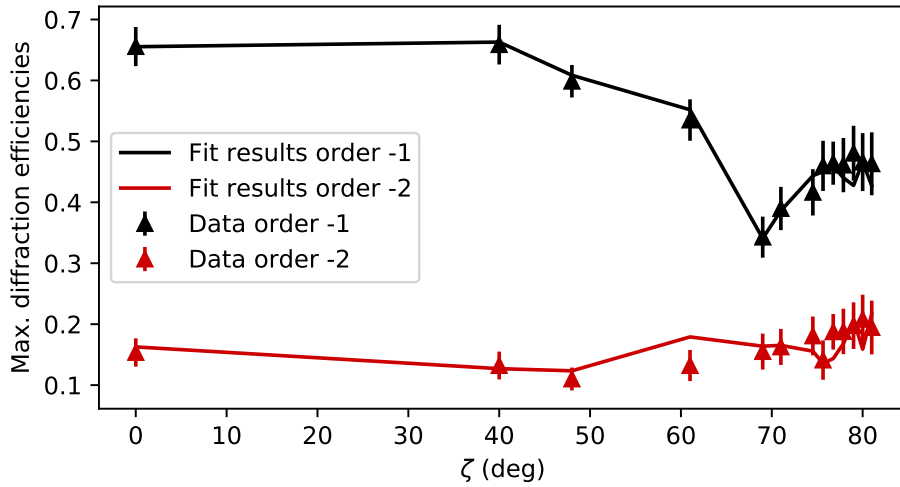


Figure 5.7: *Experimental observation of Pendellösung interference with values predicted by the fit results*

5.3 Conclusions

In general, the issues related to the experimental side can be prevented by implementing a less thorough version of the steps presented in section 4.1 at the end of each measurement session. Once the data are converted to

images, the software Fiji-ImageJ [25] offers efficient tools for a quick scan of the outcomes of the measurements. It is also feasible to generate an interface customized for the instrument that allows to directly convert the data to images and implement the preliminary analysis in a more user-friendly environment. Moreover, using He pipes with a larger diameter can avert any unwanted cut-off or increase in noise in the ROI.

Despite the analysis not being able to define common values for the scattering length-density modulation parameters and the phase, it revealed interesting features of the diffraction efficiencies and of the experiment that are worth of deeper investigation. Repeating the measurements addressing the issues brought up in this thesis might further improve the quality of the results.

Bibliography

- [1] M. G. Moharam and T. K. Gaylord. “Rigorous coupled-wave analysis of planar-grating diffraction”. In: *J. Opt. Soc. Am.* 71.7 (July 1981), pp. 811–818. DOI: 10.1364/JOSA.71.000811. URL: <http://opg.optica.org/abstract.cfm?URI=josa-71-7-811>.
- [2] Yasuo Tomita et al. “Photopolymerizable nanocomposite photonic materials and their holographic applications in light and neutron optics”. In: *Journal of Modern Optics* 63.sup3 (2016). PMID: 27594769, S1–S31. DOI: 10.1080/09500340.2016.1143534. eprint: <https://doi.org/10.1080/09500340.2016.1143534>. URL: <https://doi.org/10.1080/09500340.2016.1143534>.
- [3] T. K. Gaylord and M. G. Moharam. “Thin and thick gratings: terminology clarification”. In: *Appl. Opt.* 20.19 (Oct. 1981), pp. 3271–3273. DOI: 10.1364/AO.20.003271. URL: <http://opg.optica.org/ao/abstract.cfm?URI=ao-20-19-3271>.
- [4] Cristian Neipp et al. “Angular responses of the first diffracted order in over-modulated volume diffraction gratings”. In: *Journal of Modern Optics* 51 (May 2004), pp. 1149–1162. DOI: 10.1080/09500340408230413.
- [5] *ill.eu*. Last accessed 23/09/2022. URL: <https://www.ill.eu/>.
- [6] Jürgen Klepp et al. “Advancing data analysis for reflectivity measurements of holographic nanocomposite gratings”. In: *Journal of Physics: Conference Series* 746 (Sept. 2016), p. 012022. DOI: 10.1088/1742-6596/746/1/012022. URL: <https://doi.org/10.1088/1742-6596/746/1/012022>.
- [7] Christian Pruner et al. “Interferometer for cold neutrons”. In: *Nuclear Instruments and Methods in Physics Research Section A: Accelerators, Spectrometers, Detectors and Associated Equipment* 560.2 (2006), pp. 598–605. ISSN: 0168-9002. DOI: <https://doi.org/10.1016/j.nima.2005.12.240>. URL: <https://www.sciencedirect.com/science/article/pii/S0168900205026811>.

-
- [8] Herwig Kogelnik. “Coupled wave theory for thick hologram gratings”. In: *The Bell System Technical Journal* 48.9 (1969), pp. 2909–2947. DOI: 10.1002/j.1538-7305.1969.tb01198.x.
- [9] Naoya Uchida. “Calculation of diffraction efficiency in hologram gratings attenuated along the direction perpendicular to the grating vector”. In: *J. Opt. Soc. Am.* 63.3 (Mar. 1973), pp. 280–287. DOI: 10.1364/JOSA.63.000280. URL: <http://opg.optica.org/abstract.cfm?URI=josa-63-3-280>.
- [10] Martin Fally, Jürgen Klepp, and Yasuo Tomita. “An experimental study on the validity of diffraction theories for off-Bragg replay of volume holographic gratings”. In: *Applied Physics B* 108 (July 2012). DOI: 10.1007/s00340-012-5090-x.
- [11] Martin Fally et al. “Experimental determination of nanocomposite grating structures by light- and neutron-diffraction in the multi-wave-coupling regime”. In: *Opt. Express* 29.11 (May 2021), pp. 16153–16163. DOI: 10.1364/OE.424233. URL: <http://opg.optica.org/oe/abstract.cfm?URI=oe-29-11-16153>.
- [12] Matej Prijatelj et al. “Far-off-Bragg reconstruction of volume holographic gratings: A comparison of experiment and theories”. In: *Physical Review A* 87.6 (June 2013). DOI: 10.1103/physreva.87.063810.
- [13] Varley F. Sears. *Neutron Optics: An Introduction to the Theory of Neutron Optical Phenomena and Their Applications*. Oxford series on neutron scattering in condensed matter. Oxford University Press, 1989. ISBN: 9780195046014.
- [14] Jürgen Klepp et al. “Mirrors for slow neutrons from holographic nanoparticle -polymerfree-standing film-gratings”. In: *Applied Physics Letters* 100 (Mar. 2012), p. 214104. DOI: 10.1063/1.4720511.
- [15] TK Gaylord and MG Moharam. “Planar dielectric grating diffraction theories”. In: *Applied Physics B* 28.1 (1982), pp. 1–14. DOI: 10.1007/BF00693885.
- [16] Richard Syms and Laszlo Solymar. “Planar volume phase holograms formed in bleached photographic emulsions”. In: *Appl. Opt.* 22.10 (May 1983), pp. 1479–1496. DOI: 10.1364/AO.22.001479. URL: <http://opg.optica.org/ao/abstract.cfm?URI=ao-22-10-1479>.
- [17] Boris W. Batterman and Henderson Cole. “Dynamical Diffraction of X Rays by Perfect Crystals”. In: *Rev. Mod. Phys.* 36 (3 July 1964), pp. 681–717. DOI: 10.1103/RevModPhys.36.681. URL: <https://link.aps.org/doi/10.1103/RevModPhys.36.681>.

- [18] Clifford G. Shull. “Observation of Pendellösung Fringe Structure in Neutron Diffraction”. In: *Phys. Rev. Lett.* 21 (23 Dec. 1968), pp. 1585–1589. DOI: 10.1103/PhysRevLett.21.1585. URL: <https://link.aps.org/doi/10.1103/PhysRevLett.21.1585>.
- [19] Jürgen Klepp et al. “Three-port beam splitter for slow neutrons using holographic nanoparticle-polymer composite diffraction gratings”. In: *Applied Physics Letters* 101.15 (2012), p. 154104. DOI: 10.1063/1.4758686. eprint: <https://doi.org/10.1063/1.4758686>. URL: <https://doi.org/10.1063/1.4758686>.
- [20] Juergen Klepp et al. “Holographic gratings for slow-neutron optics”. In: *Materials* 5.12 (2012), pp. 2788–2815. URL: <https://www.mdpi.com/1996-1944/5/12/2788>.
- [21] Yasuo Tomita, Naoaki Suzuki, and Katsumi Chikama. “Holographic manipulation of nanoparticle distribution morphology in nanoparticle-dispersed photopolymers”. In: *Optics letters* 30.8 (2005), pp. 839–841.
- [22] Kurt Eder et al. “The new very-cold-neutron optics facility at ILL”. In: *Nuclear Instruments and Methods in Physics Research Section A: Accelerators, Spectrometers, Detectors and Associated Equipment* 284.1 (1989), pp. 171–175. ISSN: 0168-9002. DOI: [https://doi.org/10.1016/0168-9002\(89\)90273-8](https://doi.org/10.1016/0168-9002(89)90273-8). URL: <https://www.sciencedirect.com/science/article/pii/0168900289902738>.
- [23] Matthias Blaickner et al. “Monte-Carlo simulation of neutron transmission through nanocomposite materials for neutron-optics applications”. In: *Nuclear Instruments and Methods in Physics Research Section A: Accelerators, Spectrometers, Detectors and Associated Equipment* 916 (2019), pp. 154–157. ISSN: 0168-9002. DOI: <https://doi.org/10.1016/j.nima.2018.11.074>. URL: <https://www.sciencedirect.com/science/article/pii/S0168900218316796>.
- [24] Tatsuro Oda et al. “Towards a high-resolution TOF-MIEZE spectrometer with very cold neutrons”. In: *Nuclear Instruments and Methods in Physics Research Section A: Accelerators, Spectrometers, Detectors and Associated Equipment* 860 (2017), pp. 35–41. ISSN: 0168-9002. DOI: <https://doi.org/10.1016/j.nima.2017.03.014>. URL: <https://www.sciencedirect.com/science/article/pii/S016890021730339X>.
- [25] Johannes Schindelin et al. “Fiji: an open-source platform for biological-image analysis”. In: *Nature methods* 9.7 (2012), pp. 676–682.
- [26] Pierre Raybaut. “Spyder-documentation”. In: *Available online at: python-hosted.org* (2009).

- [27] Guido Van Rossum and Fred L. Drake. *Python 3 Reference Manual*. Scotts Valley, CA: CreateSpace, 2009. ISBN: 1441412697.
- [28] *Inverse transform sampling*. Last accessed 23/09/2022. URL: https://en.wikipedia.org/wiki/Inverse_transform_sampling.
- [29] *Statistical functions (scipy.stats)*. Last accessed 27/09/2022. URL: <https://docs.scipy.org/doc/scipy/reference/stats.html>.
- [30] *scipy.stats.exponnorm*. Last accessed 27/09/2022. URL: <https://docs.scipy.org/doc/scipy/reference/generated/scipy.stats.exponnorm.html#scipy.stats.exponnorm>.

Appendix A

A.1 Re-arranging of the coupled-waves sum

For 5 coupled waves ($m = 2$), we have

$$\begin{aligned}
& \sum_{j=-2}^2 S_j(z) \left(e^{-i(\vec{k}_{j-1} + (\delta q_{j-1} - \delta q_j)\hat{z}) \cdot \vec{r}} + e^{-i(\vec{k}_{j+1} + (\delta q_{j+1} - \delta q_j)\hat{z}) \cdot \vec{r}} \right) = \\
& = S_{-2}(z) \left(e^{-i(\vec{k}_{-3} + (\delta q_{-3} - \delta q_{-2})\hat{z}) \cdot \vec{r}} + e^{-i(\vec{k}_{-1} + (\delta q_{-1} - \delta q_{-2})\hat{z}) \cdot \vec{r}} \right) + \\
& + S_{-1}(z) \left(e^{-i(\vec{k}_{-2} + (\delta q_{-2} - \delta q_{-1})\hat{z}) \cdot \vec{r}} + e^{-i(\vec{k}_0 + (\delta q_0 - \delta q_{-1})\hat{z}) \cdot \vec{r}} \right) + \\
& + S_0(z) \left(e^{-i(\vec{k}_{-1} + (\delta q_{-1} - \delta q_0)\hat{z}) \cdot \vec{r}} + e^{-i(\vec{k}_1 + (\delta q_1 - \delta q_0)\hat{z}) \cdot \vec{r}} \right) + \\
& + S_1(z) \left(e^{-i(\vec{k}_0 + (\delta q_0 - \delta q_1)\hat{z}) \cdot \vec{r}} + e^{-i(\vec{k}_2 + (\delta q_2 - \delta q_1)\hat{z}) \cdot \vec{r}} \right) + \\
& + S_2(z) \left(e^{-i(\vec{k}_1 + (\delta q_1 - \delta q_2)\hat{z}) \cdot \vec{r}} + e^{-i(\vec{k}_3 + (\delta q_3 - \delta q_2)\hat{z}) \cdot \vec{r}} \right)
\end{aligned} \tag{A.1}$$

We can now re-arrange the terms in the following way

$$\begin{aligned}
& \sum_{j=-2}^2 S_j(z) \left(e^{-i(\vec{k}_{j-1} + (\delta q_{j-1} - \delta q_j)\hat{z}) \cdot \vec{r}} + e^{-i(\vec{k}_{j+1} + (\delta q_{j+1} - \delta q_j)\hat{z}) \cdot \vec{r}} \right) = \\
& = e^{-i\vec{k}_{-3} \cdot \vec{r}} (S_{-2}(z) e^{-i(\delta q_{-3} - \delta q_{-2})z}) + \\
& + e^{-i\vec{k}_{-2} \cdot \vec{r}} (S_{-1}(z) e^{-i(\delta q_{-2} - \delta q_{-1})z}) + \\
& + e^{-i\vec{k}_{-1} \cdot \vec{r}} (S_{-2}(z) e^{-i(\delta q_{-1} - \delta q_{-2})z} + S_0(z) e^{-i(\delta q_{-1} - \delta q_0)z}) + \\
& + e^{-i\vec{k}_0 \cdot \vec{r}} (S_{-1}(z) e^{-i(\delta q_0 - \delta q_{-1})z} + S_1(z) e^{-i(\delta q_0 - \delta q_1)z}) + \\
& + e^{-i\vec{k}_1 \cdot \vec{r}} (S_0(z) e^{-i(\delta q_1 - \delta q_0)z} + S_2(z) e^{-i(\delta q_1 - \delta q_2)z}) + \\
& + e^{-i\vec{k}_2 \cdot \vec{r}} (S_1(z) e^{-i(\delta q_2 - \delta q_1)z}) + \\
& + e^{-i\vec{k}_3 \cdot \vec{r}} (S_2(z) e^{-i(\delta q_3 - \delta q_2)z})
\end{aligned} \tag{A.2}$$

When working in an approximated model with a finite number of coupled-waves it is assumed that the components of wave vectors $k_{\pm m+1}$ are negligible, and this allows us to re-write the sum as:

$$\begin{aligned} & \sum_{j=-2}^2 S_j(z) \left(e^{-i(\vec{k}_{j-1} + (\delta q_{j-1} - \delta q_j)\hat{z}) \cdot \vec{r}} + e^{-i(\vec{k}_{j+1} + (\delta q_{j+1} - \delta q_j)\hat{z}) \cdot \vec{r}} \right) = \\ & = \sum_{j=-2}^2 e^{-i\vec{k}_j \cdot \vec{r}} \left(S_{j-1}(z) e^{-i(\delta q_j - \delta q_{j-1})z} + S_{j+1}(z) e^{-i(\delta q_j - \delta q_{j+1})z} \right) \end{aligned} \quad (\text{A.3})$$

A.2 ROI search algorithm

```

1 import numpy as np
2 matrixes = [np.loadtxt("Folder_path/file_name(j)" for j in
   range (n_measurements))]
3 #measurements in 2D array format
4
5 stack = np.stack(matrixes,axis=2)
6 #3D stack of measurements
7
8 stack_proj = np.zeros((128,128))
9 for i in range(128):
10     for j in range(128):
11         stack_proj[i,j] = np.amax(stack[i,j,:])
12 #2D projection on (x,y) of the maximum values along z
13
14 xy_max = np.where(stack_proj==np.amax(stack_proj))
15 y_max = xy_max[0][0]
16 x_max = xy_max[1][0]
17 #coordinates of the maximum of stack_proj
18
19 y1=y_max-12
20 #minimum value of the first row of the ROI
21
22 SN1=0.
23 SN2=0.
24 SN3=0.
25 while y1<y_max and (SN1<2 or SN2<2 or SN3<2):
26     N=sum(stack_proj[0:y1,x_max])/len(stack_proj[0:y1,x_max])
27     #Average noise
28     SN1=stack_proj[y1+1,x_max]/N
29     #signal to noise ratio of the pixel
30     SN2=stack_proj[y1+2,x_max]/N
31     #signal to noise ratio one pixel ahead
32     SN3=stack_proj[y1+3,x_max]/N
33     #signal to noise ratio two pixels ahead

```



```

34     y1+=1
35 y1-=1
36 #first row of the ROI

```

Algorithm A.1: Code to find the first row of the ROI based on the signal-to-noise ratio.

A.3 Fit results according to the model presented in subsec. 4.5.3

